The Hebrew University of Jerusalem

Faculty of Science

The Racach Institute of Physics

Transition from Ladder Climbing to Autoresonance

in the Flux Bias Josephson Phase Circuits

Submitted by: Ya'ara Rofe

Student number: 039884945

Supervisor: Dr. Nadav Katz

A thesis submitted for the degree of Master of Science

November, 2010

Acknowledgments

I would like to dedicate my thesis to my beloved husband Yochay and to my dear children Hallel and Yonathan. Thank you for being there for me, providing me with positive energy, cheering at every milestone, and being patient with my absence from family life.

I am grateful to my parents for encouraging me to choose the challenge of studying for a master's degree while raising a family.

My in-laws provided invaluable assistance, regularly looking after my son Yonathan, while I worked on my research.

Thanks to my colleagues from the Katz group: Yoni Shalibo, David Shwa, Felix Zaides, Ofer Fogel, Avraham Klein, Uri Vool and Nelly Segal. I appreciate the fruitful discussions and friendly atmosphere.

Thanks to Ido Barth and Professor Lazar Friedland for their cooperation on this research. They presented us with their articles, and showed us their new simulations. In addition, they followed the experiments we conducted and offered suggestions for improvement.

I would especially like to thank my supervisor, Dr. Nadav Katz for all the encouragement, guidance, patience and support from start to finish. This helped me develop an understanding of non linear quantum dynamics implemented in the Josephson phase circuits.

Abstract

In recent years, there has been a growing interest in controllable quantum systems, both for studying fundamental decoherence physics and for possibly making useful computational devices.
Our lab focuses on a solid-state implementation, based on superconducting Josephson circuits. These circuits are fabricated by modern lithography and deposition techniques borrowed from the semi-conductor industry. Superconducting circuits have the remarkable property of being non-dissipative, which is a key ingredient for observing quantum effects in a physical system.
The quantum harmonic oscillator behaves like its classical counterpart when it is in a coherent state. In fact, this is exactly what we get when exciting a resonator by classical means. However, producing non-classical states by classical means requires a nonlinear element in the circuit. Such element enables anharmonic behaviour. The Josephson junction is an element having this property.
Anharmonic oscillators exhibit a unique response to a driving force with a continuously decreasing frequency (chirped drive), referred to as autoresonance or ladder climbing in the classical or quantum regimes, respectively. The system's response, in both regimes, typically involves a bifurcation of the oscillation amplitude depending both on the strength of the drive and on the system's anharmonicity. In this parameter space, the threshold of bifurcation exhibits a transition between sequential state excitation (quantum ladder climbing) and the population of coherent-like states (classical autoresonance). Previous attempts to experimentally map the bifurcation have only been done in either classical or quantum conditions, but not in the intermediate regime.

The main goal of this work was to experimentally map these two regimes including the intermediate. Superconducting Josephson phase circuits enable us to do so in the same system, due to their tunable anharmonicity. We show a measurement of the bifurcation phenomena in this system over a large parameter space where the expected transition is observed. We compare the results to numerical simulations and to theoretical analysis and we find a good match between them.
The second goal was to develop coherent control methods. In this work we simulated

and applied a reset technique, which uses a chirped drive rather than the more traditional resonant drive (π pulse). This reset technique was found to be more robust than the resonant drive.
In this work we also set out to create a significant analytical and numerical analysis for a realistic simulation of superconducting circuits, specifically the flux-bias Josephson phase circuit.

This thesis includes five chapters. The first chapter presents a brief background as an introduction to this work (1.1), followed by detailed theoretical and numerical analyses, that I have summarized, edited and developed (1.2-1.3). The second chapter describes the research objectives. The third chapter presents the system's structure (3.1), the system components which were made by me (3.3) and the system setup (3.4). Chapter four displays the experimental results and discusses them. Chapter five summarizes this work with some closing remarks.

Contents

1 Theoretical Background **6**

1.1 Introduction 6

1.1.1 Superconductivity: flux quantization and Josephson tunnelling . 6

1.1.2 Types of Josephson circuits 8

1.1.3 Decoherence mechanisms in Josephson circuits 11

1.2 Analytical analysis 13

1.2.1 Mapping of flux-bias to current-bias circuits in a phase qubit . 13

1.2.2 From the continuous phase basis to the finite dimensional eigenbasis 15

1.2.3 Dynamics of two level systems 16

1.2.4 Chirped drive perturbation in two level systems 22

1.2.5 Chirped drive perturbation in multi level systems 27

1.3 Numerical analysis 31

1.3.1 Calculating the energies and eigenstates from the system parameters 31

1.3.2 The Hamiltonian in the RWA 32

1.3.3 Time evolution operator 32

1.3.4 Consideration of decoherence 33

2 Research Objective **34**

3 Experimental Methods **35**

3.1 System structure 35

3.1.1 Device 35

3.1.2 Sample holder 35

3.1.3 Cryogenic system 35

3.1.4 Electronics 36

3.2 System setup 37

3.3 Self made components 38

3.3.1 Copper powder filter 38

3.3.2 Sample holder 39

3.4 Course of the experiment 40
3.4.1 Calibration of the System 40
3.4.2 Measuring the qubit 44
3.4.3 Motivation and description of the experiments 46

4 Results & Discussion **47**
4.1 Linearly increasing chirped drive 47
4.2 Resonant drive 49
4.3 Linearly decreasing chirped drive 51

5 Summary & Outlook **57**

Chapter 1

Theoretical Background

1.1 Introduction

The theoretical introduction starts with a brief description of the superconductivity phenomenon including the BCS theory and the Josephson relations (1.1.1), which is based on [1]. Then, the main types of the Josephson circuits are described, with an emphasis on phase circuits (1.1.2). This last part of the introduction describes the effect of decoherence in Josephson circuits (1.1.3).

1.1.1 Superconductivity: flux quantization and Josephson tunnelling

Superconductors enable atomic- scale phenomena to be observed at the macroscopic level [2]. The reason, as explained elegantly by the theory of Bardeen, Cooper and Schrieffer [3], is that in the presence of an attractive potential and at sufficiently low temperatures, electrons near the Fermi surface become unstable against the formation of Cooper pairs. These have spin zero that enables them to form a large Bose-Einstein condensate (like bosonic particles) that is characterized by a single macroscopic state. This state is described by a wavefunction $\Psi(\mathbf{r}, t)$ (where $\mathbf{r}$ is the spatial variable and t is time). Like all quantum-mechanical wavefunctions, $\Psi(\mathbf{r}, t)$ can be written as $|\Psi(\mathbf{r}, t)| \exp[i\phi(\mathbf{r}, t)]$: that is, as the product of an amplitude and a factor involving the phase ϕ. Furthermore, in 'conventional' superconductors such as Nb, Pb and Al, the quasiparticles (electron-like and hole-like excitations) are separated in energy from the condensate by an energy gap $\Delta_s(T) = 1.76\, k_B T_C$ (where k_B is the Boltzmann constant and T_C is the superconducting transition temperature). Thus, at temperatures $T \ll T_C$, the density of quasiparticles becomes exponentially small, as does the intrinsic dissipation for frequencies of less than $2\Delta_s(0)/h$ (where h is Planck's constant), roughly

10^{11} Hz for Al.

The macroscopic wavefunction leads to two phenomena that are essential for qubits. The first phenomenon is flux quantization [4]. When a closed ring is cooled through its superconducting transition temperature in a magnetic field and the field is then switched off, the magnetic flux in the ring, maintained by a circulating supercurrent, is quantized in integer values of flux quantum $\Phi_0 \equiv h/2e \approx 2.07 \times 10^{-15}\, T\, m^2$. This quantization arises from the requirement that $\Psi(\mathbf{r}, t)$ be single valued.

The second phenomenon is Josephson tunnelling [4]. A Josephson junction consists of two superconductors separated by an insulating barrier of appropriate thickness, typically 1–2 nm, through which Cooper pairs can tunnel coherently. Brian Josephson showed [5] that the supercurrent I through the barrier is related to the gauge-invariant phase difference $\varphi(t)$ between the phases of the two superconductors by the current – phase relationship

$$I(\varphi) = I_0 sin(\varphi). \tag{1.1}$$

Here I_0 is the maximum supercurrent that the junction can sustain (that is, the critical current). This phase difference is an electrodynamic variable that, in the presence of a potential difference V between the superconductors, evolves in time as

$$\hbar\dot{\varphi} = \hbar\omega_s = 2eV, \tag{1.2}$$

where $\hbar = h/2\pi$ and ω_s is the angular frequency at which the supercurrent oscillates. The variables have, so far, been regarded as being classical, but to show quantum-mechanical behavior, these variables must be replaced by operators. The two relevant operators are that for φ, which is associated with the Josephson coupling energy $E_J = I_0\Phi_0/2\pi$, and that for the Cooper-pair number difference N across the capacitance, which is associated with the charging energy $E_C = (2e)^2/2C$, where C is the junction capacitance.

Furthermore, just like the familiar position and momentum operators[1] X and P_x, the operators for φ and for the charge on the capacitor Q are canonically conjugate, as expressed by the commutator bracket $[\varphi, Q] = i2e$. The fact that φ and Q are subject to Heisenberg's uncertainty principle has far-reaching consequences. On the one hand, when $E_J/E_C \gg 1$, φ is well defined, and Q has large quantum fluctuations; therefore, the Josephson behavior of the junction dominates. On the other hand, when $E_J/E_C \ll 1$, Q is well defined, and φ has large quantum fluctuations; therefore, the charging behavior of the capacitor dominates. Using these ideas, the parameters of superconducting quantum circuits can be designed [6].

[1] The hat sign "^" (regularly used for operators) is not used in this ducument.

1.1.2 Types of Josephson circuits

The need to reduce sensitivity of the device to noise has led to the development of three basic types of qubits. In some qubits it is possible to create states with energy that is to first order insensitive to some parameter.

Flux and phase qubits have large ratios of E_J/E_C (defined above). For these systems the energy is insensitive to charge fluctuations because the flux/phase is a well defined variable and thus the charge, being the conjugated variable has large quantum fluctuations. In this case random fluctuations in the offset charge are made negligible relative to charge fluctuations and thus eliminate its effect on the energy. In addition, flux qubits are flux biased to a symmetric potential point where the qubit energies are insensitive to flux fluctuations to first order. While phase qubits (to be discussed further hereafter) do not have such an optimal point, they have the advantage of being more tunable [7]. Charge qubits work in the opposite limit $E_C/E_J \gg 1$, where they are immune to current fluctuations. In addition, the qubit states have energies that are symmetric with respect to charge and thus to first order insensitive to charge fluctuations [7].

Newer qubits, promising greater immunity to low frequency noise are still being developed, the most prominent of them being the transmon [8]. This is a charge-phase hybrid, working in the intermediate regime $E_J \sim E_C$. As it turns out, in this regime energy-charge dispersion reduces exponentially with E_J/E_C, while (surprisingly) the relative anharmonicity, $(\omega_{23} - \omega_{12})/\omega_{12}$, reduces only algebraically, making it possible to further reduce sensitivity to charge noise in charge qubits while still being able to perform gates in relatively short times.

1.1.2.1 The current-biased Josephson junction

The Hamiltonian[2] of a current-biased Josephson junction is given by

$$H = \frac{2Q^2}{C} - E_J cos(\varphi) - \frac{\Phi_0}{2\pi} I\varphi, \tag{1.3}$$

where Q is the excess charge on the junction capacitance. The dynamics of a current biased Josephson junction are easily understood by looking at its effective potential $U(\varphi)$, plotted in Fig. 1.1(a-c). We can picture the state of the junction as being described by a fictitious particle (being composed of a macroscopic number of particles) of mass $C\left(\Phi_0/2\pi\right)^2$, moving in a one-dimensional tilted washboard potential [4].

In contrast to a linear inductor for which $\Phi = LI$ holds (Φ is the total flux through

[2]The energy is derived from the sum of electrostatic energy and the integrated power $U = \int^t IV dt$ using the Josephson relations.

the loop, L the inductance), the Josephson element satisfies $I \sim sin(\Phi_J/\Phi_0)$, where $\Phi_J \equiv \varphi\Phi_0$. Although Φ_J is not necessarily associated with a real magnetic flux, it is apparent from the above relation that this element behaves like a nonlinear inductor. In addition, every Josephson junction has a finite capacitance in parallel to its inductance. Thus at small current bias ($I \ll I_0$) it behaves like a harmonic oscillator having a resonance frequency $\omega_{p0} = 1/\sqrt{L_{J0}C}$ called the plasma frequency, where $L_{J0} = \Phi_0/2\pi I_0$ is its inductance at zero current bias [9]. At finite current bias, the frequency of classical oscillations is current dependent and we get:

$$\omega_p = \omega_{p0}\left[1 - \left(\frac{I}{I_0}\right)^2\right]^{1/4}. \tag{1.4}$$

At finite current bias $I < I_0$ the particle is trapped within one of the wells. After a characteristic relaxation time, during which it oscillates at the frequency ω_p, the phase stabilizes into a steady state value and the total current through the junction goes to zero.

If we bias the junction near its critical point $I \sim I_0$, the particle can escape by thermal activation or tunneling processes. When the particle escapes from the well, the average phase increases with time and a voltage develops across the junction according to equation (1.2). At this point the junction switches to its resistive regime, dominated by its normal resistance R_n.

The resistive characteristics of the junction can be taken into account by adding a phenomenological resistor R in parallel to the junction. In the low damping limit, where $Q_f = \omega_p RC \gg 1$ (Q_f is the quality factor) the energy levels of the circuit become much narrower than their separation and we expect quantum effects to become visible. Indeed, several groundbreaking experiments have demonstrated energy level quantization [10, 11] and macroscopic quantum tunneling [12] in this system over two decades ago. Practically, this limit is usually achieved at low temperatures, $k_BT \ll \Delta$, where the shunting resistance gets extremely large, since $R \sim R_n e^{\Delta/k_BT}$. Nevertheless, various effects additional to equilibrium quasiparticles in a superconductor contribute to dissipation, and thus to a reduction of the total quality factor of the circuit. In the section 1.1.3 we describe these processes and their origin.

Assuming that the system is at $T = 0$ and completely isolated from the environment. When the Josephson energy is dominant, $E_c \ll E_J$, the phase is a well defined variable, and therefore, it is more convenient to solve for the energy and eigenstates in the phase basis. For that reason we call this system a phase circuit. Inside each well we find quantized energy levels (Fig. 1.1(d)), where the lowest two being commonly used as a qubit. In the next section we will describe a modern version of the phase circuit that

we use in our research.

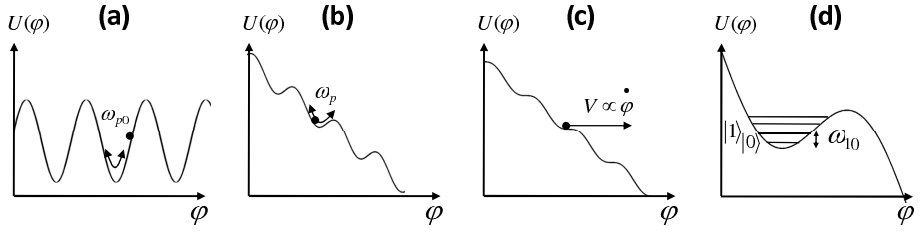

Figure 1.1: Effective potential of the current-biased Josephson junction with (a) no bias, (b) bias lower than the critical current and (c) bias equal to the critical current. (d) The quantum energy levels of a high-Q isolated system.

1.1.2.2 The flux biased Josephson phase circuit

The flux-biased phase circuit is a transformed version of the current-biased phase circuit described above, and the one that is currently being used in our work. In this circuit, instead of directly connecting the current source we used an induced current generated by a flux transformer (see Fig. 1.2(a)). This design has the advantage of providing high impedance (greater than 1MΩ instead of 50Ω) between the circuit and current source at a relatively broad frequency range [13]. Another advantage is the creation of finite number of potential wells, resulting from the quadratic potential (see Fig. 1.4). In addition, it implements a built-in single shot measurement that reduces heating of the junction and thus reduces the generation of quasiparticles. The Hamiltonian of this circuit is given by:

$$\mathcal{H} = \frac{2Q^2}{C} - \frac{I_0\Phi_0}{2\pi}cos(\varphi) + \frac{1}{2L}\left(\Phi_{ext} - \frac{\varphi\Phi_0}{2\pi}\right)^2. \tag{1.5}$$

The potential energy is plotted in Fig. 1.2(b) for a typical operating point where the flux bias (Φ_{ext}) equals nearly an integer multiple of Φ_0. At this point, a small number of energy levels exist in the left well, where the two lowest are usually used as the qubit. Although, in this research we also use multiple levels within this well.

Controlling the state of this circuit is achieved by introducing microwave currents through a small capacitor connected to the loop. The microwave signals (typically between 5 to 15 GHz) are resonant with the qubit transition and thus can be used to create arbitrary superposition of states. The microwave current is analogous to the AC magnetic field in NMR, and the evolution of the state under this signal is described

by the Bloch theory as well [14]. In a nonlinear multi-level system each transition has its own resonant frequency. Therefore, arbitrary superposition can be generated using number of different resonant frequencies.
Similar to the current-biased circuit, we measure the state by applying a short flux bias pulse that adiabatically lowers the potential barrier up to a point where the upper level is preferentially tunneled out of the well. However, unlike the current biased circuit, in this case the phase is trapped within the next well if it tunnels out and thus no DC voltage drops across the junction. Because of the fundamental relation between the phase difference across the junction and the total flux through the loop, the phase can be measured later by an on-chip superconducting quantum interference device (SQUID).

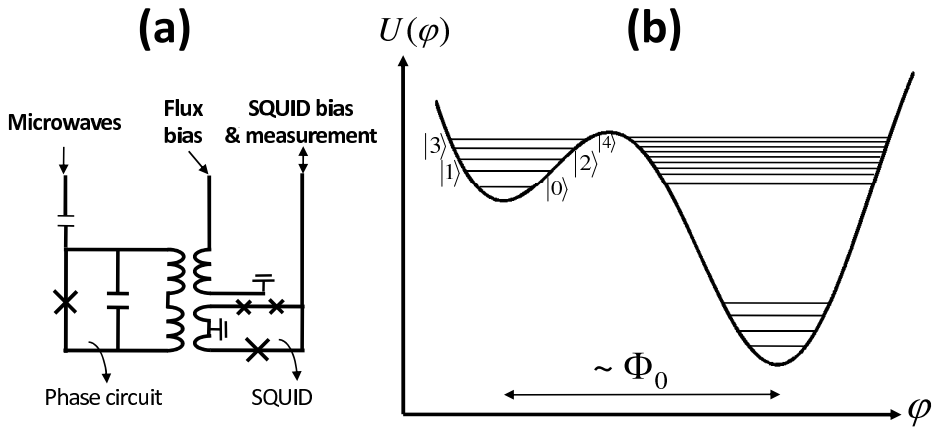

Figure 1.2: The flux-biased phase circuit. (a) circuit schematics, where x stands for a pure Josephson element. (b) effective potential with energy levels

1.1.3 Decoherence mechanisms in Josephson circuits

One of the great advantages of superconducting circuits as a tool for experimentally studying quantum effects and as quantum information processors is their macroscopic size. As macroscopic objects they are easily coupled to other circuits, but at the same time they are also more strongly coupled to their environment. The latter generally results in energy being lost from the system, and consequently in the loss of coherence.

1.1.3.1 Relaxation

Apart from equilibrium quasiparticles that exist in a superconductor at finite temperature, various processes such as thermal radiation propagating along the coax lines can

contribute to non-equilibrium excitations of quasiparticles (QPs) and thus to energy decay by resistive losses in the wires or by QPs tunneling through the junction [15].
Dielectric materials in the Josephson junction and substrate have a finite loss tangent, thus serving as a decay bath for photons in their vicinity. While low-loss materials such as c-Si and c-Al_2O_3 can be used as substrates, there is no easy method of achieving low-loss dielectrics inside junctions. In Al-Al_2O_3-Al junctions, it has been found that microscopic defects resonantly couple to the circuit and exchange energy with it during measurement [16]. Reduction of the junction area results in a smaller number of these defects, but also in reduced capacitance which has to be compensated for with a shunting capacitor having a finite loss tangent.
Control and measurement circuitry coupled to the device can dissipate its energy through current or voltage fluctuations. In a simple model, the effect of dissipation from the external circuitry can be accounted for by looking at the real part of the admittance seen by the system through an impedance transformer [17]. Using the fluctuation-dissipation theorem, a simple relation between these quantities can be derived - $ReY_{sys}(\omega) = |dI_{sys}/dI_{ext}|^2 \, ReY_{ext}(\omega)$. The bottom line here is that if fluctuation in some variable (current, voltage) of the external circuit causes fluctuation of this variable in the system, the opposite process will happen as well and this fluctuation out of equilibrium can dissipate in the external circuit.

1.1.3.2 Decoherence

Relaxation processes lead to the loss of coherence. According to the Bloch theory [14], in a two level system the dephasing rate resulting from energy relaxation is given by $\Gamma_2^r = \Gamma_1/2$, Γ_1 being the decay rate.
Quantum interaction between the system and the environment lead to non-classical correlations between the state of the system and the degrees of freedom in the environment (entanglement). As a result, the system is no longer described by a pure state having a density matrix $\rho = |\varphi\rangle \langle\varphi|$ but rather by a mixed-state having a density matrix $\rho(t) = \sum_i p_i(t) |\psi_i\rangle \langle\psi_i|$ (formally we get this by tracing out the environment from the combined system-environment density matrix) [18]. Even in the absence of relaxation processes, the off-diagonal terms in the density matrix (accounting for the coherence) can decay in time. For example, two-level defects inside the junction (mentioned above) interacting with the qubit can contribute to this type of decoherence.
A fundamentally different contribution to the loss of coherence comes from low-frequency fluctuations. The energy levels in the circuit are set by several parameters (depending on the type of circuit), such as the current bias, and critical current in the current-biased circuit. When these parameters fluctuate, a random phase is accumulated

$\phi(t) = \int^t \omega(t')dt'$, and thus the state dephases relative to the control pulses which (ideally) retain phase correlation between themselves. It should be emphasized that this kind of dephasing is classical, since it results from noise in a classical parameter of the system.

In flux and phase qubits, the large loop inductance leads to great sensitivity to flux. In current phase qubits, flux fluctuations were found to be the dominant cause for dephasing [19]. In a separate work it was found that flux fluctuations result from magnetic defects - presumably in the native oxide covering the superconducting wires [20]. In charge qubits, fluctuations in the offset charge are more deleterious and result from local charges in the junction, quasiparticles tunneling across the junction and Johnson-Nyquist noise at finite temperature. In both cases the noise scales with frequency as $1/f$ so there is a significant dephasing at long times, making it harder to perform long experiments or increase the measurement statistics by repeating the experiment many times.

1.2 Analytical analysis

This section contains the detailed theoretical and numerical analysis that has been done in the framwork of this research. In 1.2.1 the Hamiltonian of the flux-bias Josephson phase circuit is mapped to that of the current-bias circuit, which allows use of the standard current bias theory for the case of the flux bias. Then, 1.2.2 shows the transformation between the phase basis of the Hamiltonian to its finite dimensional subspace, followed by the general dynamics of two level systems (1.2.3), based on [21]. It continues with a detailed discussion of a chirped pulse perturbation dynamics in two level systems (1.2.4), based on [22]. The second part ends with the special case of decreasing chirped pulse in multi level systems considering classical or quantum conditions, referred to as autoresonance or ladder climbing, respectively. The conditions for the transition from the quantum to the classical regimes are outlined [23].

1.2.1 Mapping of flux-bias to current-bias circuits in a phase qubit

The theory of the phase qubit is typically modeled with a current-bias circuit. Therefore, mapping the flux-bias circuit to a current-bias circuit allows use of the standard current bias theory for the case of the flux biased junction [24]. This is done by modifying the effective junction critical current and bias current. In Fig. 1.3 (A) the circuit of the current-biased Josephson junction is shown. The potential describing this circuit

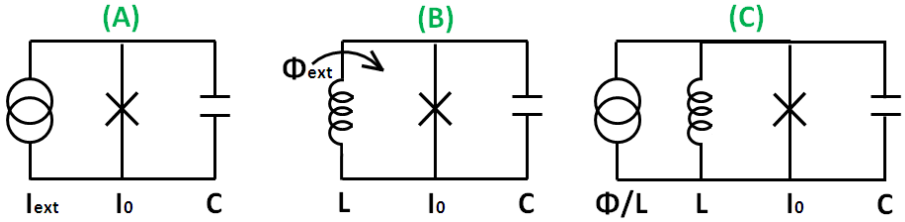

Figure 1.3: (A) Circuit diagram for the current-biased Josephson junction. (B) Circuit for the flux-biased junction. (C) Thevenin equivalent circuit of (B).

with bias source I_{ext} and junction critical current I_0 is:

$$U_{current}(\varphi) = -\frac{I_0\Phi_0}{2\pi}\cos\varphi - \frac{I\Phi_0}{2\pi}\varphi, \tag{1.6}$$

The magnitude of the potential barrier approaches zero as the bias approaches the critical bias, which can be defind as the critical phase $\varphi_0$where

$$\left[\frac{\partial^2 U_{current}(\varphi)}{\partial\varphi^2}\right]_{\varphi_0} = \left[\frac{\partial U_{current}(\varphi)}{\partial\varphi}\right]_{\varphi_0} = 0. \tag{1.7}$$

The second derivative of $U_{current}(\varphi)$ is zero at the critical phase $\varphi_0 = \pi/2$. This requirement is also fulfilled at $\varphi = \varphi_0 + \pi n$, which reflects the potential period, 2π, and the freedom to choose the direction (sign) of the current bias. For positive current bias the inflection point near the edge of the well occurs at its right side, which corresponds to $\varphi = \varphi_0 + \pi(2n)$, and for negative current bias it occurs the left side, which corresponds to $\varphi = \varphi_0 + \pi(2n+1)$. Expanding the potential around φ_0 with $\varphi = \varphi_0 + \varphi'$, and ignoring constant terms we find

$$U'_{current}(\varphi') = \frac{\Phi_0}{2\pi}\left[I_0\sin\varphi' - I\varphi'\right]. \tag{1.8}$$

Fig. 1.3(**A**) shows the circuit for the flux-biased Josephson junction. The potential for this circuit with a loop inductance L is

$$U_{flux}(\varphi) = -\frac{I_0\Phi_0}{2\pi}\cos\varphi + \frac{1}{2L}\left[\Phi_{ext} - \frac{\varphi\Phi_0}{2\pi}\right]^2 \tag{1.9}$$

The second derivative of $U_{flux}(\varphi)$ is zero at a critical phase $\varphi_0 = -L_{J0}/L$, where $L_{J0} = \Phi_0/2\pi I_0$ is the Josephson inductance of the junction at zero bias. Expanding the potential around φ_0 with $\varphi = \varphi_0 + \varphi'$, and ignoring constant terms we find

$$U'_{flux}(\varphi') = \frac{\Phi_0}{2\pi}\left[(I_0\sin\varphi_0)\sin\delta' - (\frac{\Phi_{ext} - \delta_0\Phi_0/2\pi}{L})\varphi'\right]. \tag{1.10}$$

Now we can notice that this equation is identical to the potential for the current-biased Josephson junction Eq.1.8, but with the "renormalization" of parameters,

$$I_0^{eff} = I_0 \sin\varphi_0,\ I^{eff} = \frac{\Phi_{ext} - \varphi_0\Phi_0/2\pi}{L}. \tag{1.11}$$

The magnitude of the potential barrier approaches zero as I^{eff} approaches I_0^{eff}. This yields the critical flux Φ_C,

$$\Phi_C = \frac{\Phi_0}{2\pi}(\varphi_0 - \tan\varphi_0). \tag{1.12}$$

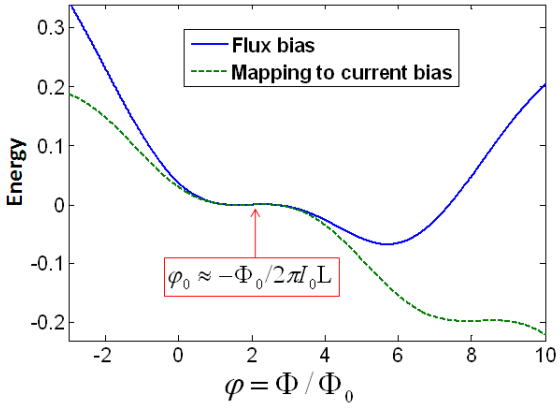

Figure 1.4: The potential of the flux bias circuit is approxmated to the potential of the current bias circuit around the inflection point, φ_0.

1.2.2 From the continuous phase basis to the finite dimensional eigenbasis

In order to understand the dynamics of the states in the qubit well (which is the most shallow well of the potential), one could first approximate the potential to a simpler form, and than diagonalize the Hamiltonian in the phase space. The resulting eigenvalues and eigenvectors are the energies and eigenfunctions, respectively. The number of levels in the well that are taking into account, n, determines the dimension of the Hamiltonian subspace.

$$H_0 = \begin{bmatrix} E_0 & & & \\ & E_1 & & \\ & & \ddots & \\ & & & E_n \end{bmatrix} \tag{1.13}$$

In the current bias phase circuit, when the bias current is slightly smaller than the critical current, $I_{ext} \leq I_0$, the potential, Eq.(1.6), can be accurately approximated by a cubic potential $U(\varphi)$, parametrized by a barrier height $\Delta U(I) = (2\sqrt{2}I_0\Phi_0/3\pi)\,[1 - I/I_0]^{3/2}$ and a quadratic curvature at the bottom of the well that gives a classical oscillation frequency $\omega_P(I) = 2^{1/4}\,(2\pi I_0/\Phi_0 C)^{1/2}\,[1 - I/I_0]^{1/4}$ [9]. The commutation relation $[\varphi, Q] = i2e$ leads to quantized energy levels in the cubic potential [25]. Microwave bias currents induce transitions between levels at a frequency $\omega_{mn} = E_{mn}/\hbar = (E_n - E_m)/\hbar$, where E_n is the energy of state $|n\rangle$. The two lowest transitions have frequencies

$$\omega_{01} \simeq \omega_P \left(1 - \frac{5}{36}\frac{\hbar\omega_P}{\Delta U}\right), \tag{1.14}$$

$$\omega_{12} \simeq \omega_P \left(1 - \frac{10}{36}\frac{\hbar\omega_P}{\Delta U}\right). \tag{1.15}$$

The ratio $\Delta U/\hbar\omega_P$ parametrizes the anharmonicity of the cubic potential with regard to the qubit states, and gives an estimate of the number of states in the well. In the presence of a forcing drive with small driving amplitude I_{mw} and a driving frequency ω_d, the Hamiltonian takes the form

$$H = \begin{bmatrix} E_0 & & & \\ & E_1 & & \\ & & \ddots & \\ & & & E_n \end{bmatrix} - \frac{\Phi_0}{2\pi} I_{mw}(t) cos(\int \omega_d(t)dt) \begin{bmatrix} \langle 0|\,\varphi\,|0\rangle & \langle 0|\,\varphi\,|1\rangle & \dots & \langle 0|\,\varphi\,|n\rangle \\ \langle 1|\,\varphi\,|0\rangle & \langle 1|\,\varphi\,|1\rangle & & \\ \vdots & & \ddots & \\ \langle n|\,\varphi\,|0\rangle & & & \langle n|\,\varphi\,|n\rangle \end{bmatrix} \tag{1.16}$$

where the first term on the right side of the equal sign is the unperturbed Hamiltonian, and the second term is the perturbation term. According to calculations in the non perturbed system when the cubic potential is valid, the elements $\langle n|\,\varphi\,|m\rangle$ are calculated [25]. The elements along the first upper and lower diagonals increase approximately as $\sim \sqrt{n}$ (similar to harmonic oscillator). In the next section we will consider the case of a two dimensional Hamiltonian.

1.2.3 Dynamics of two level systems

In this section we will show the dynamics of two level systems. This can be suitable for either real two level systems or for highly nonlinear multi level systems, in which the resonance frequencies are significantly separated.

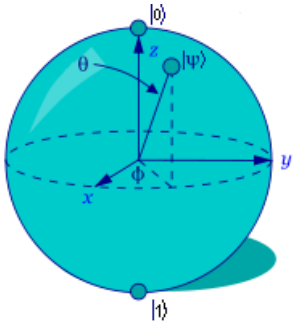

Figure 1.5: The Bloch sphere: Points on the sphere correspond to the quantum state $|\psi\rangle$; in particular, the north and south poles correspond to the basis states $|0\rangle$ and $|1\rangle$; superposition cat-states $|\psi\rangle = |0\rangle + e^{i\phi}|1\rangle$are situated on the equator.

1.2.3.1 The state evolution on the Bloch sphere

A quantum bit (qubit), is a two-level quantum system described by the state vector

$$|\psi\rangle = \cos\frac{\theta}{2}|0\rangle + \sin\frac{\theta}{2}e^{i\phi}|1\rangle \tag{1.17}$$

Expressing $|0\rangle$ and $|1\rangle$ in terms of the eigenvectors of the Pauli matrix $\sigma_z = \begin{pmatrix} 1 & 0 \\ 0 & -1 \end{pmatrix}$,

$$|0\rangle \equiv \begin{pmatrix} 1 \\ 0 \end{pmatrix}, |1\rangle \equiv \begin{pmatrix} 0 \\ 1 \end{pmatrix}. \tag{1.18}$$

this can be described as a rotation from the north pole of the $|0\rangle$ state.

$$|\psi\rangle = \begin{pmatrix} 1 & 0 \\ 0 & e^{i\phi} \end{pmatrix} \begin{pmatrix} \cos\frac{\theta}{2} & \sin\frac{\theta}{2} \\ \sin\frac{\theta}{2} & \cos\frac{\theta}{2} \end{pmatrix} \begin{pmatrix} 1 \\ 0 \end{pmatrix} \tag{1.19}$$

The state vector can be represented as a unitary vector on the Bloch sphere, as shown in Fig. 1.5. Notice that the Bloch sphere is twice the angle of the Dirac notation. The dynamics on the Bloch sphere is conveniently described in terms of the density matrix. For a pure quantum state,

$$\rho = |\psi\rangle\langle\psi| \tag{1.20}$$

This is a 2×2 Hermitian matrix whose diagonal elements ρ_{11} and ρ_{22} define occupation probabilities of the basis states, hence satisfying the normalization condition: $\rho_{11}+\rho_{22} = 1$, while the off-diagonal elements give information about the phase. The density matrix can be mapped on a real 3-vector by means of the standard expansion in terms of σ-

matrices: $\sigma_x = \begin{pmatrix} 0 & 1 \\ 1 & 0 \end{pmatrix}$, $\sigma_y = \begin{pmatrix} 0 & -i \\ i & 0 \end{pmatrix}$ and $\sigma_z = \begin{pmatrix} 1 & 0 \\ 0 & -1 \end{pmatrix}$,

$$\rho = \frac{1}{2}\left(\hat{1} + \rho_x\sigma_x + \rho_y\sigma_y + \rho_z\sigma_z\right), \tag{1.21}$$

introduced in Fig. 1.5 ($\hat{1}$ is the identity matrix $\hat{1} = \begin{pmatrix} 1 & 0 \\ 0 & 1 \end{pmatrix}$). Direct calculation of the density matrix Eq.(1.20) using Eq.(1.17) and comparing with Eq.(1.21) shows that the vector $\boldsymbol{\rho} = (\rho_x, \rho_y, \rho_z)$ coincides with the Bloch vector,

$$\boldsymbol{\rho} = (\sin\theta\cos\phi, \sin\theta\sin\phi, \cos\theta) \tag{1.22}$$

In the same σ- matrix basis, the general two-level Hamiltonian takes the form[3]

$$H = \left(H_x\sigma_x + H_y\sigma_y + H_z\sigma_z\right), \tag{1.23}$$

giving a 3-vector representation for the Hamiltonian,

$$\mathbf{H} = (H_x, H_y, H_z). \tag{1.24}$$

The time evolution of the density matrix is given by the Liouville equation,

$$i\hbar\partial_t\rho = [H, \rho]. \tag{1.25}$$

The vector form of this equation is readily derived by inserting Eqs.(1.21)-(1.24) into Eq. (1.25) and using the commutation relations among the Pauli matrices,

$$\partial_t\boldsymbol{\rho} = \frac{1}{\hbar}(\mathbf{H} \times \boldsymbol{\rho}) \tag{1.26}$$

This equation coincides with the Bloch equation for a magnetic moment evolving in a magnetic field. The role of the magnetic moment being played by the Bloch vector ρ which rotates around the effective "magnetic field" $H-$associated with the Hamiltonian of the qubit (plus any driving fields).

1.2.3.2 DC-pulses

To control the dynamics of the qubit system, one method is to apply dc (square) pulses which suddenly change the Hamiltonian and, consequently, the time evolution operator. Sudden pulse switching means that the time-dependent Hamiltonian is changed so fast

[3]In this form the constant element of the Hamiltonian proportional to the Unit operator is excluded because it only displaces the energy levels, but doesn't affect the state evolution.

on the time scale of the state vector evolution, that the state vector can be treated as "frozen" during the switching time interval. Then the state vector begins to evolve in time under the influence of the new Hamiltonian. A two-level Hamiltonian in the σ-matrix basis has the form[4]

$$H = H_z\sigma_z + H_x\sigma_x \tag{1.27}$$

Now, let us can consider the stationary case, where $H_x = \eta = const$ and $H_z = -\epsilon = const$. The qubit eigenstates are to be found from the stationary Schrödinger equation

$$\hat{H}\,|\psi\rangle = E\,|\psi\rangle \tag{1.28}$$

To solve this equation we expand the qubit state in the σ_z eigenstates (1.18),

$$|\psi\rangle = \langle 0|\psi\rangle\,|0\rangle + \langle 1|\psi\rangle\,|1\rangle \tag{1.29}$$

Then we get the Hamiltonian matrix

$$\hat{H} = \begin{pmatrix} -\epsilon & \eta \\ \eta & \epsilon \end{pmatrix} \tag{1.30}$$

Finally after some straightforward manipulation we get the solutions for the eigenvalues Eq.(1.28), which are energies and eigenstates,

$$E_{1,2} = \pm\sqrt{\epsilon^2 + \eta^2} \tag{1.31}$$

$$|E_1\rangle = \frac{1}{\sqrt{2}}\sqrt{1 + \frac{\epsilon}{\sqrt{\epsilon^2+\eta^2}}}\,|0\rangle + \frac{1}{\sqrt{2}}\sqrt{1 - \frac{\epsilon}{\sqrt{\epsilon^2+\eta^2}}}\,|1\rangle \tag{1.32}$$

$$|E_2\rangle = \frac{1}{\sqrt{2}}\sqrt{1 - \frac{\epsilon}{\sqrt{\epsilon^2+\eta^2}}}\,|0\rangle - \frac{1}{\sqrt{2}}\sqrt{1 + \frac{\epsilon}{\sqrt{\epsilon^2+\eta^2}}}\,|1\rangle \tag{1.33}$$

The general solution is a combination of the eigenstates with phases corresponding to their energies.

$$|\psi\rangle = \cos\frac{\theta'}{2}\,|E_1\rangle\,e^{-iE_1t/\hbar} + \sin\frac{\theta'}{2}\,|E_2\rangle\,e^{-iE_2t/\hbar} \tag{1.34}$$

θ' is obtained from boundary conditions. On the Bloch sphere it describes free precession around the direction defined by the energy eigenbasis with constant angular speed $(E_1 - E_2)/\hbar$. If the system is driven to the degeneracy point $\epsilon = 0$ then for initial

[4]Without lose of generality, we chose the off diagonal element to be real.

condition $|\psi(0)\rangle = |0\rangle$ the probability of finding the system in state $|1\rangle$ oscillates like

$$P_2(t) = |\langle 1|\psi\,(t)\rangle|^2 = \frac{1}{2}\left[1 - \cos((E_2 - E_1)t/\hbar)\right] \tag{1.35}$$

and the precession is around the X-axis.
In principle, using dc- pulses it is possible to reach every state, but the oscillations are very fast, and therefore are too hard to control.

1.2.3.3 Harmonic perturbation and Rabi oscillations

A particularly interesting and practically important case concerns harmonic perturbation with small amplitude λ and frequency around the resonant frequency ω_d. In the σ-matrix basis the Hamiltonian has the form,

$$H = H_z\sigma_z + H_x\sigma_x, \tag{1.36}$$

where $H_x = \eta = \lambda\cos\omega_d t$ and $H_z = -\hbar\omega_0/2 = const.$ In the eigenbasis of the non-pertubed qubit, $|E_1\rangle$ and $|E_2\rangle$ the Hamiltonian will take the form:

$$H = \begin{pmatrix} -\hbar\omega_0/2 & \lambda\cos\omega_d t \\ \lambda\cos\omega_d t & \hbar\omega_0/2 \end{pmatrix} \tag{1.37}$$

In spite of the amplitude being small, $\lambda/\hbar\omega_0 \ll 1$, the system will be driven far away from the initial state because of the resonance. The dynamics of the states is obtained from the time dependent Schrödinger equation

$$i\hbar\frac{\partial|\psi\rangle}{\partial t} = H|\psi\rangle. \tag{1.38}$$

In order to solve it let us switch into a rotating wave frame (RWF) [14]

$$|\psi\rangle \to |\widetilde{\psi}\rangle = V|\psi\rangle. \tag{1.39}$$

The Hamiltonian corresponding to $|\widetilde{\psi}\rangle$ is

$$H \to \widetilde{H} = VHV^\dagger - i\hbar V\frac{\partial V^\dagger}{\partial t}. \tag{1.40}$$

Inserting $V = \begin{pmatrix} e^{-i\omega_d t/2} & \\ & e^{i\omega_d t/2} \end{pmatrix}$ into Eqs. (1.39) and (1.40) we get

$$|\widetilde{\psi}\rangle = a(t)e^{-i\omega_d t/2}\,|E_1\rangle + b(t)e^{i\omega_d t}\,|E_2\rangle \tag{1.41}$$

$$\widetilde{H} = \begin{pmatrix} -\hbar(\omega_o - \omega_d)/2 & \lambda\cos\omega t e^{-i\omega_d t} \\ \lambda\cos\omega t e^{i\omega_d t} & \hbar(\omega_o - \omega_d)/2 \end{pmatrix}. \tag{1.42}$$

Inserting $\cos\omega_d t = (e^{i\omega_d t} + e^{-i\omega_d t})/2$ and $\omega_d = \omega_0 - \delta$ (δ is the detuning) we get,

$$\widetilde{H} = \frac{1}{2}\begin{pmatrix} -\hbar\delta & \lambda \\ \lambda & \hbar\delta \end{pmatrix} + \begin{pmatrix} 0 & \frac{1}{2}\lambda e^{-2i\omega t} \\ \frac{1}{2}\lambda e^{2i\omega t} & 0 \end{pmatrix}. \tag{1.43}$$

Now we can notice that the first term is constant, while the second one changes very fast (about twice the resonant frequency), so we can substitute it by its average over a period, which is zero. This is called the "rotating wave approximation" (RWA) [14].

$$\widetilde{H}_{RWA} = \frac{1}{2}\begin{pmatrix} -\hbar\delta & \lambda \\ \lambda & \hbar\delta \end{pmatrix} \tag{1.44}$$

The Hamiltonian in this basis (the "dressed states" basis) is time independent so we can use the solutions from the previous paragraph, Eqs.(1.31), (1.32), (1.33). The energy spacing and the coupling are replaced by the detuning and the driving amplitude in the following way: $\epsilon = \hbar\delta/2$ and $\eta = \lambda/2$.

$$E_\pm = \pm\frac{1}{2}\sqrt{\lambda^2 + (\hbar\delta)^2} \tag{1.45}$$

$$|E_\pm\rangle = \frac{1}{\sqrt{2}}\sqrt{1 \pm \frac{\hbar\delta}{\sqrt{\lambda^2 + (\hbar\delta)^2}}}\,|E_1\rangle \pm \frac{1}{\sqrt{2}}\sqrt{1 \mp \frac{\hbar\delta}{\sqrt{\lambda^2 + (\hbar\delta)^2}}}e^{i\omega t}\,|E_2\rangle \tag{1.46}$$

The general solution is a combination of the eigenstates with phases corresponding to their energies.

$$|\psi\rangle = \cos\frac{\theta'}{2}\,|E_+\rangle\,e^{-iE_+ t/\hbar} + \sin\frac{\theta'}{2}\,|E_-\rangle\,e^{-iE_- t/\hbar} \tag{1.47}$$

θ' is obtained from boundary conditions. On the Bloch sphere, in the RWF, it describes free precession around the direction defined by the energy eigenbasis. The rotation frequency is $\Omega_{rabi} = (E_+ + E_-)/\hbar = \sqrt{\lambda^2 + (\hbar\delta)^2}/\hbar$, where $\Omega_{rabi} \ll \omega_0$. For instance,

if δ=0 the rotation is around the X axis and the rotation frequency is $\Omega_{rabi} = \lambda/\hbar$, which is the rate of the population transfer between ground and excited states. The probability of being in one of the states oscillates as a function of time. These oscillations are called Rabi oscillations and the oscillations frequency is called Rabi frequency. If we apply a drive pulse of a duration such that $\Omega_{rabi}(t-t_0) = \pi$ the populations of the ground state and the excited state will flip - such a pulse is called a π-pulse. Another useful pulse is the $\frac{\pi}{2}$-pulse which brings the ground state to the "equator".

1.2.4 Chirped drive perturbation in two level systems

Chirped pulse perturbation concerns a small harmonic perturbation with a dynamically changed frequency $\omega_d(t) = \omega_0 - \delta(t)$, which is a generalization of the Rabi perturbation, discussed above. This is also a generalization of the Landau-Zener model [26] for a constant coupling of a finite duration. The exact evolution matrix is expressed in terms of sums of by-products of parabolic cylinder functions estimated at the turn-on time and at the turn-off time of the coupling. Various approximations in terms of simpler functions are derived and applied to several physically distinct cases. They allow us to study the dependence of the transition probability on the interaction parameters: coupling strength, coupling duration, and detuning slope. The discussion is based mainly on the article [22]. In the previous paragraph we saw that using the RWA, the problem of two constant energy levels with harmonic perturbation can be mapped to a two level system with an energy gap equal to the detuning and a coupling term equal to the driving amplitude. In particular, a linear chirp $\delta(t) = \alpha t$ where α is a constant chirp rate, can be mapped to a linear change in the energy gap. The Hamiltonian in the RWF after the RWA takes the form:

$$H = \hbar \begin{pmatrix} -\Delta(t) & \Omega(t) \\ \Omega(t) & \Delta(t) \end{pmatrix}, \tag{1.48}$$

Relating to previous notation, Eq.1.44, $\Delta(t) = \delta(t)/2$ and $\Omega(t) = \lambda/\hbar 2$. We consider the case of a linearly chirped pulse with a constant coupling of a finite duration:

$$\Omega(t) = \begin{cases} \Omega_0, & t_i \leq t_f \\ 0, & else \end{cases}, \Delta(t) = v^2 t, \tag{1.49}$$

with $v^2 = \alpha/2$. The chirp sequence is shown in Fig. 1.6.

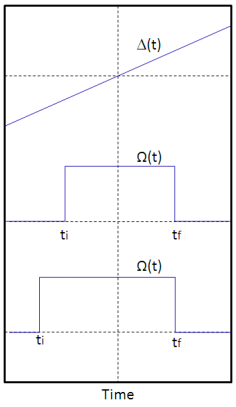

Figure 1.6: Chirp sequence: Top-detuning; Middle- symmetric coupling duration; Bottom- asymmetric coupling duration

The time dependent Schrödinger equation for the probability amplitudes $C_1(t)$ and $C_2(t)$ is:

$$i\frac{d}{dt}C_1(t) = -\Delta(t)C_1(t) + \Omega(t)C_2(t) \tag{1.50}$$

$$i\frac{d}{dt}C_2(t) = \Omega(t)C(t) + \Delta(t)C_2(t). \tag{1.51}$$

1.2.4.1 Exact solution for finite Landau-Zener model

The solution for Eqs.(1.50,1.51) in expressed in new variables: $T = \upsilon t$ and $\Lambda = \Omega/\upsilon$, which are dimensionless time and coupling strength. The probability amplitudes $C_1(T_f)$ and $C_2(T_f)$ at the final time T_f are connected to their values $C_1(T_i)$ and $C_2(T_i)$ at the initial time T_i by the evolution matrix $\mathbf{U}(T_f, T_i)$:

$$\overrightarrow{C}(T_f) = \mathbf{U}(T_f, T_i)\overrightarrow{C}(T_i), \tag{1.52}$$

where $\overrightarrow{C}(T) = \begin{pmatrix} C_1(T) \\ C_2(T) \end{pmatrix}$ is probability amplitudes vector. The elements of $\mathbf{U}(T_f, T_i)$ are:

$$U_{11}(T_f, T_i) = U_{22} * (T_f, T_i) = \left[\frac{\Gamma(1 - \frac{1}{2}i\Lambda^2)}{\sqrt{2\pi}}\right] \times$$

$$\left[D_{i\Lambda^2/2}(T_f\sqrt{2}e^{-i\pi/4})D_{i\Lambda^2/2-1}(T_i\sqrt{2}e^{i3\pi/4}) + D_{i\Lambda^2/2-1}(T_f\sqrt{2}e^{i3\pi/4})D_{i\Lambda^2/2-1}(T_i\sqrt{2}e^{-i\pi/4})\right] \tag{1.53}$$

$$U_{12}(T_f, T_i) = -U_{21} * (T_f, T_i) = \left[\frac{\Gamma(1 - \frac{1}{2}i\Lambda^2)}{\Lambda\sqrt{\pi}}e^{i\pi/4}\right] \times$$

$$\left[-D_{i\Lambda^2/2}(T_f\sqrt{2}e^{-i\pi/4})D_{i\Lambda^2/2}(T_i\sqrt{2}e^{i3\pi/4}) + D_{i\Lambda^2/2}(T_f\sqrt{2}e^{i3\pi/4})D_{i\Lambda^2/2}(T_i\sqrt{2}e^{-i\pi/4})\right] \tag{1.54}$$

This solution is general, and applies to any initial condition. If the system is initialized to the ground state,

$$C_1(t_i) = 1,\ C_2(t_i) = 0, \tag{1.55}$$

the exact transition probability is

$$P_{exact}(T_f, T_i) = \frac{1}{2\sinh\frac{1}{2}\pi\Lambda^2}\times$$

$$\left|-D_{i\Lambda^2/2}(T_f\sqrt{2}e^{-i\pi/4}) \times D_{i\Lambda^2/2}(T_i\sqrt{2}e^{i3\pi/4}) + D_{i\Lambda^2/2}(T_f\sqrt{2}e^{3\pi/4}) \times D_{i\Lambda^2/2}(T_i\sqrt{2}e^{-i\pi/4})\right|^2. \tag{1.56}$$

D are the parabolic cylinder functions, which solve the Weber equation [27].

Approximations to the transition probability In this part we are going to consider different approximations to the transition probability that are valid in different ranges of the chirp parameters. The first one is the classical Landau-Zener (LZ) model that is a particular case where T_i and T_f are infinitely large. The second one is the adiabatic-following approximation, which is valid when either the coupling strength is large, or the chirp rate is slow. The last one is the weak coupling approximation which is valid for small amplitudes. The exact solution and the approximations are shown in Fig. 1.7.

1.2.4.2 Classical Landau-Zener model

The Classical LZ model is an exact solution in the limits $T_i \to -\infty$ and $T_f \to +\infty$. Zener [26] made a similar analysis to the one shown in the previous paragraph, and found the particular parabolic cylinder functions that solve the Weber equation for infinitely large times under the boundary conditions (1.55), which gives the known solution [5]

$$P_{trans} = 1 - \exp(-\pi\Omega^2/\upsilon^2) \tag{1.57}$$

This solution is valid for large T_i and T_f, and arbitrary Ω.

[5] That is the Zener formula, while Landau has obtained a similar formula having a too small exponent by a factor of 2π [26].

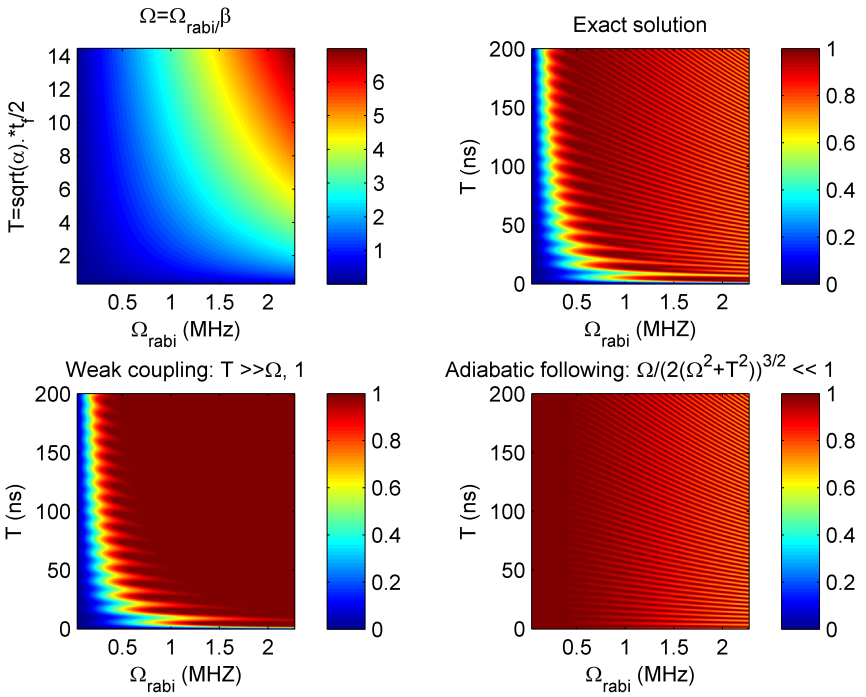

Figure 1.7: Finite LZ. Top-left: relevant parameters; Top-right: exact solution; Bottom: weak coupling and adiabatic following approximations;

1.2.4.3 Adiabatic-following solution

In the adiabatic limit the Hamiltonian is changed so slowly on the time scale of the state evolution, that the state "follows" the dynamic Hamiltonian (in the temporary eigenbasis it is almost diagonal). That means that no transitions are induced, and the system stays in the same energy level (although the state changes). The adiabatic solution can be obtained by transforming Eqs.(1.50),(1.51) into the adiabatic representation by the unitary transformation

$$\mathbf{C}(T) = \mathbf{R}(T)\mathbf{A}(T), \tag{1.58}$$

where $\mathbf{A}(T)$ is the probability amplitudes vector, and $\mathbf{R}(T)$ is the rotation matrix,

$$\mathbf{R}(T) = \begin{pmatrix} \cos\theta(T) & \sin\theta(T) \\ -\sin\theta(T) & \cos\theta(T) \end{pmatrix}. \tag{1.59}$$

The Hamiltonian transforms to the RWF according to

$$\widetilde{H} = RHR^{\dagger} - i\hbar R\frac{\partial R^{\dagger}}{\partial t}. \tag{1.60}$$

Inserting Eqs. (1.48) and 1.59into Eq.(1.60), we get

$$\widetilde{H} = \hbar \begin{pmatrix} -\sqrt{\Delta^2(T)+\Omega^2} & +i\theta'(T) \\ -i\theta'(T) & -\sqrt{\Delta^2(T)+\Omega^2} \end{pmatrix}, \tag{1.61}$$

Where $\theta(T) = -\frac{1}{2}\arctan(\Omega/\Delta(T))$ and $\theta'(T) = +\frac{1}{2}\upsilon^2\Omega/(\Delta^2(T)+\Omega^2)$.
When the diagonal elements are much larger than the off diagonal ones, we get the condition for the adiabatic following approximation

$$\frac{\Lambda}{2(\Lambda^2+T^2)^{3/2}} \ll 1. \tag{1.62}$$

That applies for $\Lambda \gg 1$ and for $T \gg \Lambda$. The time dependent Schrödinger equation (Eq.1.38) for the Hamiltonian in the adiabatic following approximation is

$$i\frac{\partial \mathbf{A}}{\partial t} = \begin{pmatrix} -\sqrt{\Delta^2(T)+\Omega^2} & 0 \\ 0 & -\sqrt{\Delta^2(T)+\Omega^2} \end{pmatrix} \mathbf{A}. \tag{1.63}$$

The solution is:

$$\mathbf{A}(T_f) = \mathbf{U_a}(T_f, T_i)\mathbf{A}(T_i), \tag{1.64}$$

where $\mathbf{U_a}(T_f, T_i)$ is the time evolution matrix in the adiabatic basis.

$$\mathbf{U_a}(T_f, T_i) = \begin{bmatrix} e^{-i\zeta_a(T_i,T_f)} & 0 \\ 0 & e^{+i\zeta_a(T_i,T_f)} \end{bmatrix} \tag{1.65}$$

where

$$\zeta_a(T_f, T_i) = \int_{T_i}^{T_f} \sqrt{T^2+\Lambda^2}dT = \frac{1}{2}\left(T_f\sqrt{T_f^2+\Lambda^2} - T_i\sqrt{T_i^2+\Lambda^2}\right) + \frac{\Lambda^2}{2}\ln\frac{T_f+\sqrt{T_f^2+\Lambda^2}}{T_i+\sqrt{T_i^2+\Lambda^2}}. \tag{1.66}$$

The evolution matrix in the original diabatic representation is:

$$\mathbf{U}(T_f, T_i) = \mathbf{R}(T_f)\mathbf{U_a}(T_f, T_i)\mathbf{R}^T(T_i). \tag{1.67}$$

Thus, we find the adiabatic-following solution for the transition probability
$P_{adiabatic}(T_f, T_i) = |\mathbf{U}_{21}(T_f, T_i)^2|$,

$$P_{adiabatic}(T_f, T_i) \approx \frac{1}{2} + \frac{T_iT_f}{2\sqrt{\left(T_i^2+\Lambda^2\right)\left(T_f^2+\Lambda^2\right)}} - \frac{\Lambda^2}{2\sqrt{\left(T_i^2+\Lambda^2\right)\left(T_f^2+\Lambda^2\right)}}\cos 2\zeta_a(T_f, -T_i). \tag{1.68}$$

For a symmetric case $T_f = -T_i = T$ we get

$$P_{adiabatic}(T,-T) = 1 - \frac{\Lambda^2}{T^2+\Lambda^2}\cos^2\zeta_a(T,T), \tag{1.69}$$

One can notice that taking the limits of infinitely large times we get the classical LZ solution.

1.2.4.4 Weak-coupling asymptotics

The transition probability for asymmetric crossing in the weak - coupling approximation, that is valid when $T \gg \omega$ and $T \gg \omega$ is:

$$P_{weak}(T,-T) \sim 1 - e^{-\pi\Lambda^2} - \frac{2\Lambda}{T}e^{-\pi\Lambda^2/2}\sqrt{1-e^{-\pi\Lambda^2}}\cos\xi_\Lambda(T), \tag{1.70}$$

where $\xi_\Lambda(T) = \frac{\Lambda^2}{2}\ln 2T^2 + T^2 + \frac{\pi}{4} + \arg\Gamma(1-\frac{1}{2}\Lambda^2)$.

1.2.5 Chirped drive perturbation in multi level systems

The analysis of our system in the presence of a chirped drive perturbation is complicated. However, there are two distinct cases in which we can simplify the analysis: the classical autoresonance model and the quantum ladder climbing model. The autoresonance phenomenon allows excitation of a classical oscillatory nonlinear system by using a weak chirped frequency force. The analog phenomenon in quantum mechanics is the ladder climbing. Conditions for the transition from the quantum to the classical regimes are described in [22]. These two phenomena involve a bifurcation of the states occupation. When a driven force is applied on a system initially in the ground state, for low enough amplitudes the states occupation is not affected. As the amplitude is increased peak separation begins. At very high amplitudes the entire occupation is phase-locked with the chirped drive and moves with the chirp rate in the energy space. The difference between auto-resonance and ladder climbing can be measured using the expectation value of the systems energy $\langle H \rangle$. For auto-resonance the movement is continuous while for ladder climbing it is discrete. At intermediate amplitudes, the occupation is divided between the lower and higher energy peaks. The lower energy peak behaves as a system feeling a small driving force (low amplitude), i.e. remains in the ground state. The higher energy peak behaves as a system feeling a strong driving force (high amplitude), i.e. moves along with the chirp rate. Therefore, during the process we can observe an increase in the peak separation. This energy gap between the peaks increases with the chirp rate. When the amplitude of the chirp drive is increased the higher energy peak fraction increases, and accordingly the lower energy peak fraction

decreases. The bifurcation process is the separation of the occupation into the two peaks. We define the bifurcation threshold as the curve in the chirp parameters space for which the population is divided equally between the peaks. The bifurcation cutoff is defined as the middle of the energy gap between the peaks. The states above the cutoff are called "latched", although this definition can be ambiguous in the case of an incomplete bifurcation.

1.2.5.1 Classical dynamic autoresonance

Dynamic autoresonance (AR) is a method of exciting an oscillatory nonlinear system to high energies by a weak driving oscillation, as well as controlling the excited state by changing the driving frequency. In the absence of noise there are two mathematical solutions, bounded and unbounded ones. The transition between these solutions is controlled by single parameter $\mu = \varepsilon/\alpha^{3/4}$, where ε is the driving amplitude and α is the chirp rate. It was found numerically that $\mu_{th} = 0.41$ is the threshold value in which above it the phase locking persists and the amplitude grows continuously, while below it the excitation dephases from the drive and saturates. The critical amplitude follows a power low: $\varepsilon_{th} \propto \alpha^{3/4}$. Considering the presence of thermal noise, this threshold expands and we get a finite width bifurcation threshold [28]. The width of the bifurcation at low temperatures is also limited by quantum noise of the ground state, due to the uncertainty principle.

1.2.5.2 Quantum mechanical ladder climbing

As a result of the anharmonicity of the potential well the energy differences between neighboring levels, $E_n - E_{n-1} = \omega_{n-1,n}$ decreases at higher energy levels, and so correspond to decreasing resonant frequencies, where $\omega_{n-1,n} > \omega_{n,n+1}$. These resonant frequencies in the quantum mechanical regime are very distant from each other, and have no overlap between them. Therefore, an external drive (having one frequency) can only be in resonance with one of the transitions and so the dynamics of the system can be approximated to that of a two level system, with the other levels staying unaffected. Therefore, applying a decreasing chirped drive (having a continuously decreasing frequency) to the system initialized to the ground can lead to a cascade of discrete transitions from the initial to the final state through a series of intermediate levels. This process can be illustrated as ladder climbing in the energy space. The climbing from one ladder step to another is done in a LZ manner, meaning that the system occupies a certain energy level until it reaches a resonance frequency and then a short transition to the neighboring level occurs. Due to the discreteness of the ladder climbing, the population fraction which is phase locked to the drive and moving along

with the chirp rate is localized mainly in the highest (significantly) occupied energy level. Therefore in this regime the occupation of this energy level can show the bifurcation phenomenon, where occupation of 50% is defined as the bifurcation threshold. The effective coupling of neighboring energy levels increases as the square root of the state number $\sqrt{n}$, like in a harmonic oscillator. Considering a two level system, the probability of staying in the initial state after a LZ perturbation (as mentioned in 1.2.4.2), is

$$P_{diabatic}(n) = \exp(-\pi\Omega_n^2/\nu^2) \approx \exp(-\pi(\Omega\sqrt{n})^2/\nu^2) \tag{1.71}$$

The probability of consecutive transitions from $|0\rangle$ to$|N \gg 1\rangle$ is

$$P_{trans}(N \gg 1) = \prod_{n=1}^{N}(1-q^n) = (1-q^1)(1-q^2)(1-q^3)... \approx 1-q-q^2+O(q^5), \tag{1.72}$$

with $q = 1 - P_{diabatic}(1)$. Therefore, requiring $P_{trans}(N \gg 1) = \frac{1}{2}$ leads to the condition of the bifurcation threshold,

$$\pi\Omega^2/\nu^2 = 1, \tag{1.73}$$

where $\pi\Omega^2/\nu^2 > 1$ means that larger occupation fraction is "latched" by the chirped drive.

1.2.5.3 Transition from LC to AR

The perturbation of a linearly decreasing chirped drive in non-linear systems has three relevant time scales: the Rabi time scale T_R, the sweep rate time scale T_S, and the nonlinear transition time scale T_{NL}. These time scales are defined as follows:

$$T_R = 1/\Omega_R,\ T_S = 1/\sqrt{|\alpha|},\ T_{NL} = 2\omega_0\beta_q/|\alpha| \tag{1.74}$$

where Ω_R is the Rabi angular frequency, $\alpha = 2\nu^2$ is the chirp rate and $\omega_0\beta_q = \omega_{01} - \omega_{12}$. In these terms, the ladder climbing threshold can be expressed as

$$T_S/T_R = \sqrt{2/\pi}. \tag{1.75}$$

The autoresonance threshold can be expressed as

$$T_R^2/(T_S T_{NL}) = 1.48. \tag{1.76}$$

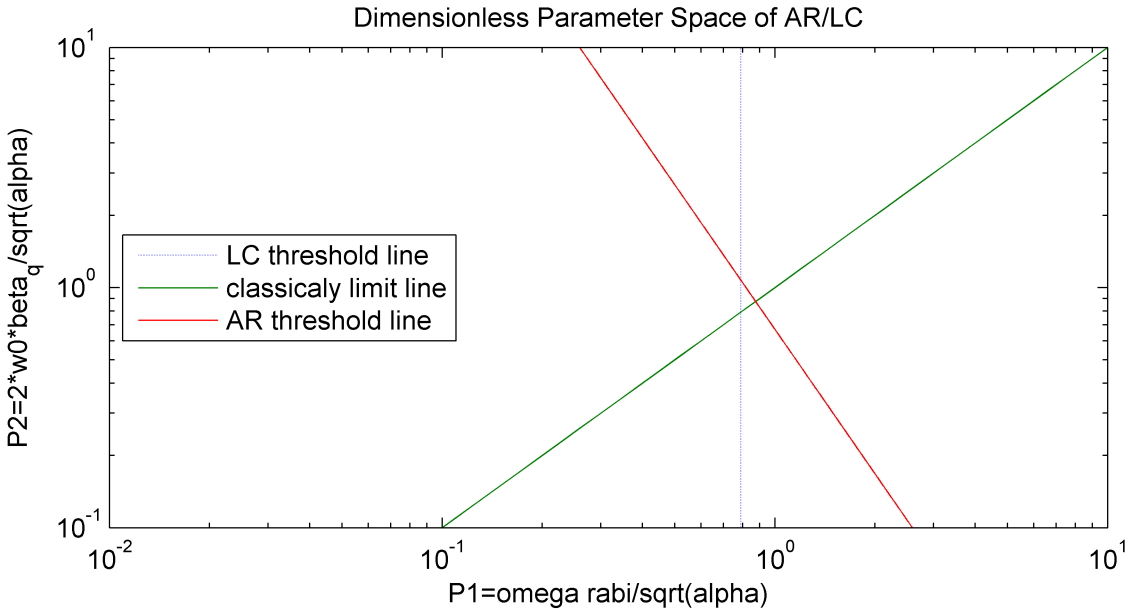

Figure 1.8: Transition between ladder climbing and autoresonance

The number of levels mixed by the driving force distinguishes between the classical and the quantum regimes. The classical - quantum limit is expressed as:

$$T_S^2/(T_R T_{NL}) = 1 \tag{1.77}$$

It is comfortable to visualize the different regimes in the two dimensionless parameters [23]:

$$P_1 = T_S/T_R \; end \; P_2 = T_{NL}/T_S. \tag{1.78}$$

Eqs.(1.75-1.77) are transformed to the three following equations:

$$P_1 = 0.79, \tag{1.79}$$

$$P_2 = P_1, \tag{1.80}$$

$$P_2 = 0.67/P_1^2. \tag{1.81}$$

Fig. 1.8 presents the critical curves is the dimensionless parameter space in a log-log scale.

1.3 Numerical analysis

1.3.1 Calculating the energies and eigenstates from the system parameters

The first part of the simulation involves receiving the parameters of the circuit and translating them into the energies and eigenvectors of the qudit. The Hamiltonian of the flux biased Josephson phase circuit is given by

$$H = -\frac{I_0\phi_0}{2\pi}cos\varphi + \frac{1}{2L}[\phi_{ext} - \varphi\frac{\phi_0}{2\pi}]^2 + \frac{2}{C}Q^2,$$

where δ and Q are the superconducting phase difference across the junction and the charge, respectively. C, L, ϕ_{ext} and I_0 are parameters of the circuit representing the junction capacitance, loop inductance, flux bias and critical current, respectively. $\phi_0 = \frac{h}{2e}$ is the superconducting flux quantum.

The simulation works in the phase basis, and first chooses a discrete grid for the phase. When the Hamiltonian is written as an operator in the phase basis, the potential is diagonalized because it's already in the phase basis. The kinetic energy, on the other hand, is in the charge basis. Due to the commutation relation, $[\varphi, Q] = 2ei$, the charge is represented as a derivative in the phase basis, $Q = -2ei\frac{d}{d\varphi}$, so $\hat{Q}^2$ corresponds to a second derivative, which in a discrete approximation becomes a term in the 3 main diagonals,

$$\frac{d^2}{dx^2}\begin{bmatrix} f(x_1) \\ f(x_1) \\ \vdots \\ \vdots \\ \vdots \\ f(x_N) \end{bmatrix} \approx \frac{1}{(\Delta x)^2}\begin{bmatrix} \ddots & \ddots & & & & \\ \ddots & -2 & 1 & & & \\ & 1 & -2 & 1 & & \\ & & 1 & -2 & 1 & \\ & & & 1 & -2 & \ddots \\ & & & & \ddots & \ddots \end{bmatrix}\begin{bmatrix} f(x_1) \\ f(x_1) \\ \vdots \\ \vdots \\ \vdots \\ f(x_N) \end{bmatrix}. \tag{1.82}$$

The energies are the eigenvalues of the Hamiltonian matrix that are calculated by using advanced numerical methods.

Once the energies are found, the simulation chooses the energies within the desired potential well, and calculates their corresponding eigenvectors (eigen functions) numerically. Among them we are looking for the "trapped" eigenfunctions, whose expected value is a phase within the well, $\langle\psi_i(\varphi)\,|\varphi|\,\psi_i(\varphi)\rangle < \varphi_0$, where φ_0 is the Inflection point close to the edge of the well. Then we choose the number of levels we want to consider, n (the level of the qudit), so we get the n lowest energies and their corresponding

eigenvectors.

1.3.2 The Hamiltonian in the RWA

Now that we have the energies and eigenvectors of the Hamiltonian - we basically have the Hamiltonian of the n-level system as a diagonal matrix. To this Hamiltonian, we add a drive element representing a time varying external current that flows into the circuit. With this addition the Hamiltonian takes the form:

$$H(t) = \begin{bmatrix} E_0 & & & \\ & E_1 & & \\ & & \ddots & \\ & & & E_n \end{bmatrix} - I_{mw}(t)cos(\int \omega(t)dt + \phi)\frac{\phi_0}{2\pi} \begin{bmatrix} \langle 0|\varphi|0\rangle & \langle 0|\varphi|1\rangle & \dots & \langle 0|\varphi|n\rangle \\ \langle 1|\varphi|0\rangle & \langle 1|\varphi|1\rangle & & \\ \vdots & & \ddots & \\ \langle n|\varphi|0\rangle & & & \langle n|\varphi|n\rangle \end{bmatrix}$$

Where $I_{mw}(t)$ is the envelope of the external current with a dynamic frequency ω and initial phase ϕ. The Hamiltonian is transformed into the frame rotating clockwise with frequency ω, where the transformation matrix is: $V_{ext} = \begin{bmatrix} 1 & & & \\ & e^{i\omega t} & & \\ & & \ddots & \\ & & & e^{in\omega t} \end{bmatrix}$.

The transformation is similar to 1.40. At this point we neglect elements that vary with time like $e^{i\omega t}$ or faster, this approximation is called the rotating wave approximation (RWA). The Hamiltonian after the approximation takes the form:

$$H_{RWA}(t) = \begin{bmatrix} 0 & & & \\ & \Delta_{01} & & \\ & & \ddots & \\ & & & \Delta_{0n} \end{bmatrix} + I(t)\frac{\phi_0}{4\pi} \begin{bmatrix} 0 & \varphi_{01}e^{i\varphi} & & 0 \\ \varphi_{10}e^{-i\varphi} & 0 & \ddots & \\ & \ddots & \ddots & \varphi_{n,n-1}e^{i\varphi} \\ 0 & & \varphi_{n-1,n}e^{-i\varphi} & 0 \end{bmatrix}$$

Where $\Delta_{0k} = E_k - E_0 - k\hbar\omega$ and $\varphi_{mn} = \langle m|\varphi|n\rangle$.
If we don't approximate the Hamiltonian, we will have to use a very small time step (less than $2\pi/\omega$) since the Hamiltonian varies with frequency ω . Moving into the external and applying the RWA the system doesn't vary with frequencies of multiplies of ω, but only slow changes depends on the signal's chirp and shape.

1.3.3 Time evolution operator

After building the Hamiltonian as a function of time, we can construct the time evolution operator and simulate the evolution of the system. The simulation constructs an

initial density matrix representing the state at the beginning of the simulation - usually set to the ground state. Then at every time step it calculates the time evolution operator as $U(t) = e^{-iH(t)\Delta t/\hbar}$ and applies it on the density matrix $\rho(t + \Delta t) = U(t)\rho(t)U(t)^{\dagger}$.

1.3.4 Consideration of decoherence

At every time step the simulation also applies the Kraus operators [18] fitting the selected T_1 and T_2 times for each transition level. The decay times of the first excited state are measured experimentally. The coupling element of neighboring levels grow like $\sqrt{n}$, n being the state number. The decay times for high levels go like the square of the coupling element; therefore, they are taken to be n times shorter. Using the time evolution operator and the Kraus operators, we finally, get the dynamics of the system.

Chapter 2

Research Objective

The main subject of this work is controllable quantum systems. These systems can be used for both studying fundamental decoherence physics and towards making useful computational devices. Our lab focuses on the flux bias Josephson phase circuit, which is a good candidate due to its tunable anharmonicity, as discussed earlier.

The main goal of this work is to experimentally map classical and quantum regimes including the intermediate regime. We use the bifurcation phenomena of a driven anharmonic oscillator since it has unique property for each regime. Sequential state excitation characterizes the quantum regime (ladder climbing), and the population of coherent-like states characterize the classical regime (autoresonance). The different regimes can be characterized by a different bifurcation threshold. Previous attempts to experimentally map the bifurcation have only been done in either classical [29] or quantum [30] regimes, but not in the intermediate regime. In our system classical and quantum behavior can be obtained by changing the anharmonicity of the system (the flux bias).

We want to find a correlation between experimental results and theoretical predictions in the classical regime and in the quantum regime. We also want to generate a realistic simulation that would fit to a continuous transition between classical and quantum regimes.

Our second goal is to develop working methods, numerical and experimental to work with anharmonic oscillators. We want to build a simulation that can be used as a numerical description of realistic anharmonic oscillators, in order to develop control methods. We want to show that a linearly increasing chirped drive can be used as a control method for state preparation. We want to show that this method is more robust than using a resonant drive.

Chapter 3

Experimental Methods

This chapter is divided into three parts. The first part (3.1) contains the system's structure. The second part (3.3) describes the system components which were handmade by me, and the third part (3.4) discusses the course of the experiment.

3.1 System structure

3.1.1 Device

The device contains the flux bias Josephson phase circuit and the Superconducting QUantum Interference Device (SQUID) (see Fig. 3.1 also sketched in Fig. 1.2). The substrate is Sapphire with size $(6.25) \times (6.25) \times (0.5)\, mm^3$. The SQUID measures the phase difference across the Josephson junction.

3.1.2 Sample holder

The sample holder houses the device at its center, and has six entries of coaxial cables enabling conducting experiments on to two qubits. It is made of Aluminum (which is known for its low resistance at these temperatures).

3.1.3 Cryogenic system

The cryogenic system – Oxford-Vericold dilution refrigerator, reaches a base temperature of 10 milli-Kelvins (mK), in which thermal excitation of states in the phase circuit are suppressed. It contains several concentric height differentiated plates (as can be seen in Fig. (3.1), right). Each plate has different temperature, the lower the plate the smaller and cooler it is. The cooling down to 10mK is done using He3/He4 mixture in a closed cycle. It allows us to perform continuous, long (>month) experiments at low

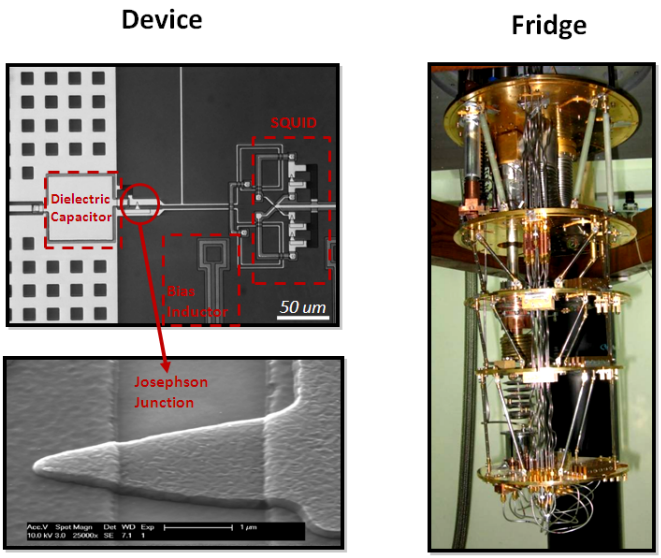

Figure 3.1: Left - Top- Optical micrograph of the device used in our measurements. At the bottom the Josephson junction enlarged. Samples were fabricated at UCSB (Martinis group); Right - Oxford-Vericold dilution refrigerator without the Mu-metal covers.

cost and without any outside interference throughout its operation. It is covered by three concentric Mu-metal cans screening magnetic fields.

3.1.4 Electronics

The system is controlled and measured by electronic devices through the computer.

3.1.4.1 Channels controlling and measuring the System

The flux bias and microwaves channels both control the qudit's state. The flux bias channel works at low frequencies and induces a potential bias, while the microwave channel works at high frequencies (typically between 5 to 15 GHz), inducing transitions between the states. The third channel is connected to the SQUID and reads the qudit's state.

3.1.4.2 Filters

Our system contains a number of filters, aimed to prevent signals in undesired frequencies. Among them: Gaussian filters, copper powder filters, and other low pass filters.

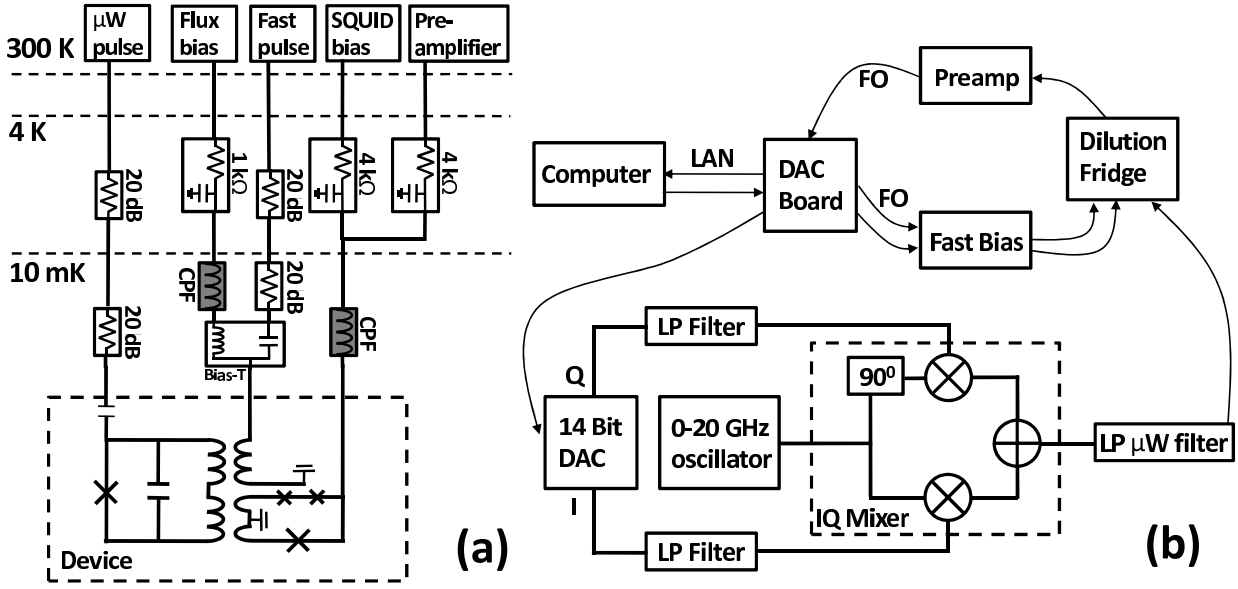

Figure 3.2: Experimental apparatus. (a) Fridge wiring and filtering. (b) Control and measurement electronics. Lower part: Microwave pulse generation.

3.2 System setup

We connect the chip to the coaxial cables through an adjusting, hexagonal shaped, PCB board having 50Ω impedance. The connection between the chip and the PCB board is done using a special wire bonder in the nano center and the connection between the PCB and the cables is done by soldering.

Then, we connect the sample holder to the coldest plate of the fridge. There are several filters located in different places of the fridge, between the chip device and the room temperature electronics, in order to attenuate undesired frequencies and noise. The fridge wiring and filtering is shown schematically in Fig. 3.2 (a). The fridge is connected to control and measurement electronics via coaxial cables. The whole system is connected through the DAC board to the computer, where the output signals pass also through a preamplifier (see Fig. 3.2 (b)). When the system setup is complete the experiments are fully controlled and measured through the computer.

3.3 Self made components

3.3.1 Copper powder filter

This is a low pass filter that sits in the refrigerator in order to prevent undesired thermal noise entry at high frequencies (GHz) coming from the environment into the refrigerator through the cables [31].
Filter structure: Since working with high frequencies requires the use of coaxial cables and SMA connectors, the filter has a coaxial structure, and two SMA connectors, from both sides.
The filter is composed of the elements shown in Fig. (3.3):

A. Two SMA connectors

B. One copper coil

C. A copper case

D. Epoxy (insulator) copper powder mixture (with tens of microns grain size

We chose to create a box composed of four filters, in order to save space in the refrigerator. The structure of this filters device is based upon the work done by Martinis group from Santa Barbara.

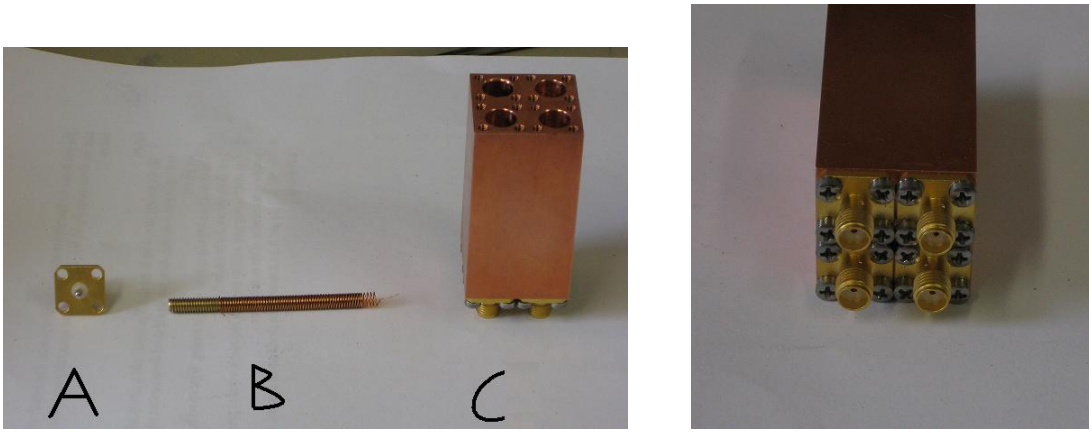

Figure 3.3: Copper powder filter: Left- parts: A. squared SMA connector; B. copper wire, wound on a screw to create the coil; C. copper case with four filters. Right: The complete device of four filters.

The copper grains absorb high frequencies by the skin effect.
In Fig. (3.4), you can see the transmission of two samples of four filters, including 10 and 75 microns sized copper powder. Indeed, we achieved the desired behavior of the

filter. The cut off frequency is around 0.5 GHz. The transmission decreases to -90 dB, between 3 and 9.5 GHz, and then reaches saturation with value of -50 dB.

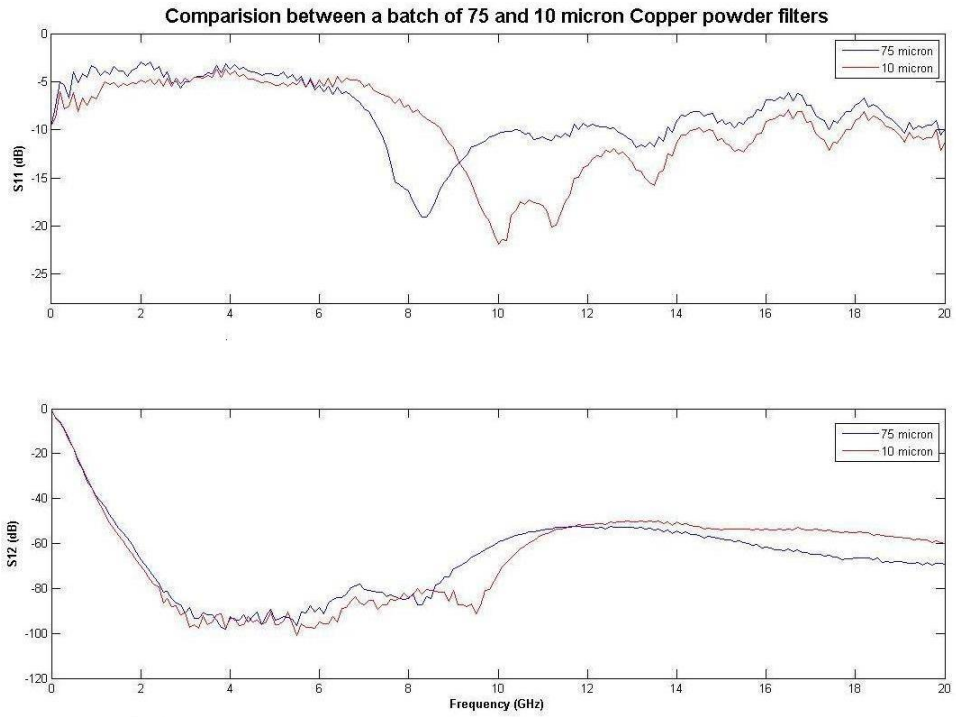

Figure 3.4: Copper powder filters: upper - reflection; lower - transmission.

From a comparison between filters with grain sizes 75 and 10 microns, we see that on average, the later show wider range of low transmission (reaches almost 10 GHz), and after the saturation it is more constant but has a little bit higher transmission.

3.3.2 Sample holder

The sample holder is composed of the following elements, as shown in the Figure below:

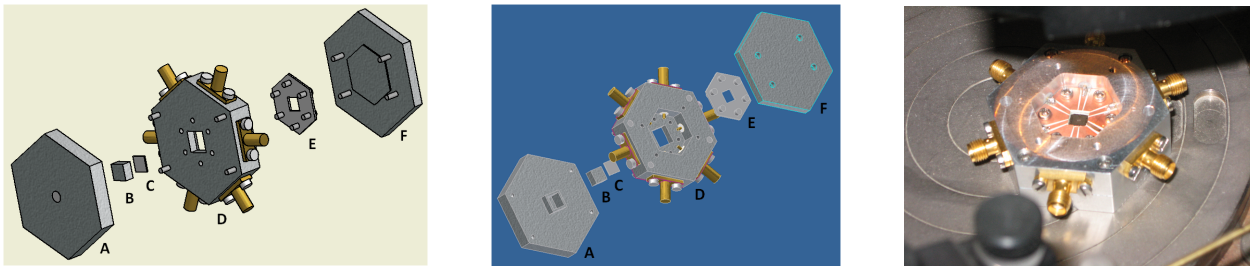

Figure 3.5: Sample holder picture and illustrations form two points of view including the following parts: A. base; B. aluminum plate; C. chip; D. Main part containing 6 SMA connectors; E. PCB ; H. cover

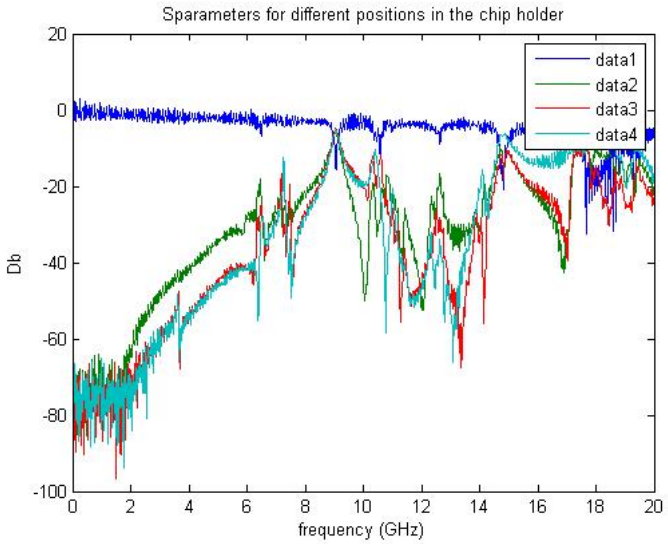

Figure 3.6: blue-0^0,green-60^0, red-120^0, light blue-180^0

The transmission and reflection of the device as measured using Network Analyzer are shown in the following Figure:

3.4 Course of the experiment

This section describes the main steps of the system calibration, the measurement process and the experiments that have been done in the framework of this research.

3.4.1 Calibration of the System

3.4.1.1 Potential landscape

In order to find the potential landscape we sweep through the biasing flux and measure the phase state after it relaxes to one of the wells, using the on-chip SQUID. Repeating such a measurement many times reveals a series of slanted branches (SQUID steps) that correspond to stable potential wells. At flux biases close to a critical flux Φ_c a certain well becomes unstable and the phase can escape to a lower energy well by tunneling[1]. This happens at a branch edge.

[1]The conditions in our experiments (bath temperature, characteristic currents and normal resistances) are similar to those reported elsewhere[12], where it was found that thermal activation is negligible.

3.4.1.2 Resetting the qubit

Before conducting the experiment, we want to ensure that the phase is localized in the qubit well at the beginning of each experiment. We do so by sweeping periodically between flux biases for which the only stable well (branch) throughout the sweep is the one we wish to localize the phase in (see figure 3.7). The sweep period is taken to be the time it takes for the current in the loop to relax into steady state (phase gets trapped within a well), which is typically a few microseconds. After a sufficient amount of repetitions the phase can be localized in the particular well with probability that is arbitrarily close to one, depending on the time we're willing to put into this procedure. The number of repetitions of the potential tilt depends on the number of stable potential wells. A smaller number of potential well requires fewer repetitions. The specific circuit we use has only two stable potential wells, so the reset is quite short. At smaller flux biases (closer to the center of the branch), the well is deeper and thus the phase is localized. As the external flux is increased, the well becomes shallower and tunneling out of the well increases the probability of escape.

3.4.1.3 Qubit spectroscopy

We do spectroscopy measurements on the qubit in order to find its resonant frequency as a function of Φ_{ext}. This is done by applying a long microwave pulse ($\tau_{pulse} \gg T_1, T_2$) saturating the transition, followed by a measurement of P_1. In this case, Bloch theory for a two level system predicts that the excited state probability should vary with the detuning as a Lorenzian, given by:

$$P_1(\delta) = \frac{T_1 T_2' \Omega^2}{1 + (\delta T_2')^2 + T_1 T_2' \Omega^2} \tag{3.1}$$

Where $\delta = \omega_d - \omega_{01}$ is the detuning, T_1 is the relaxation time, T_2' is the homogeneous dephasing time and Ω is the Rabi frequency.
We find in this sweep multiple peaks corresponding to multi-photon transitions at frequencies corresponding to E_{n0}/nh with up to $n = 4$. Figure 3.8 shows a spectroscopy sweep of the one-photon transition, identified by the highest frequency peak in the spectrum (we do not observe the direct E_{20} transition because it is beyond our frequency range for the current device).

The center of spectrum at each flux bias is derived from a fit to equation 1.4. The spectral peaks fit this formula very well. Small deviations seen at the edges are due to neglecting of the second term in the expression for $E_{10}(\Phi)$ which is proportional to a small fraction of $\frac{\hbar\omega_p}{\Delta U}$. We see that the transition frequency can be tuned by almost 20 % with the bias changed by less than $0.1\,\Phi_0$ or 0.018 the size of a branch. The only

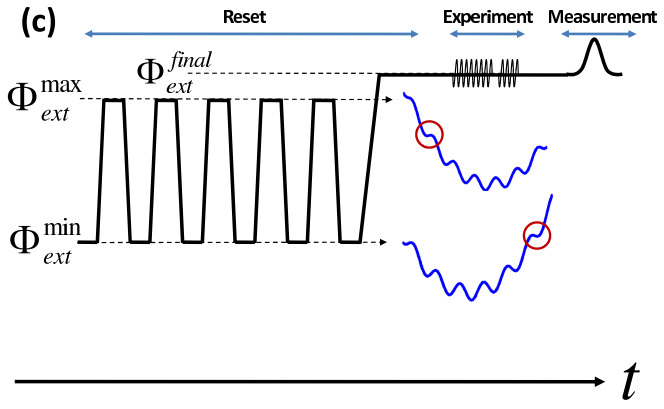

Figure 3.7: The experiment sequence start with a reset pulse, continues with the desired experimental pulse, which is followed by a measurement pulse. An illustration of the reset sequence showing the flux biases and their corresponding circuit potentials. The final wells, where the phase gets trapped after the reset are indicated by red circles. All the stable wells to the left of the encircled well at flux Φ_{ext}^{max} become unstable at Φ_{ext}^{min}. Similarly, all the stable wells to the right of the encircled well at flux Φ_{ext}^{min} become unstable at Φ_{ext}^{max}. The only stable well throughout the process is the one indicated.

limit on the tunability comes from the maximal amplitude that we can achieve with our currently implemented measurement pulse. So we'll be able to expand the tunability by using a high frequency broadband amplifier. We also observe splittings as large as 20 MHz in magnitude, that arise from coupling of the circuit to small defects in the junction dielectric that are resonant with the qubit at a particular flux bias [16]. During a measurement pulse, the qubit is tuned in- and off-resonance with several defects which may absorb its energy, thereby reducing the measurement fidelity. If the pulse is fast enough, there is a higher probability of "tunneling" through the splittings in a Landau-Zener process[32]. In small area junctions (such as in this device) their number is greatly reduced, but they still affect the measurement fidelity[33]. The spectra were measured at the low-power limit ($\Omega_{Rabi}^2 \ll \Gamma_2'\Gamma_1$) where power broadening is negligible. In this limit the linewidth is determined only by the dephasing time: $\Delta f_{FWHM} = 1/\pi T_2'$, according to equation 3.1. We find linewidths of size $\Delta f \simeq 7$ MHz taken as the full width at half maximum, corresponding to a dephasing time of $\simeq 50$ ns which is smaller than the one we measure in the Ramsey experiment (see below).

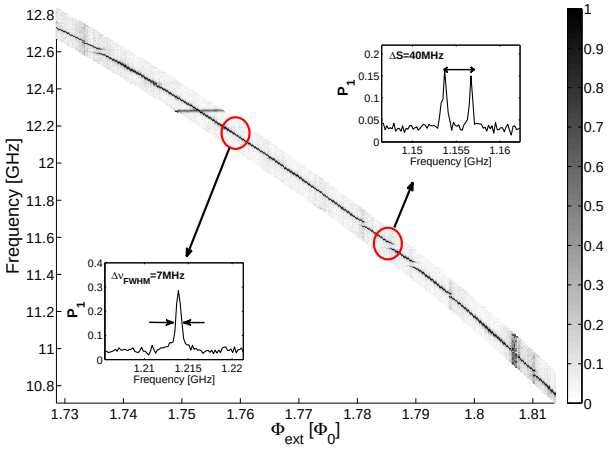

Figure 3.8: Spectroscopy sweep of the $|0\rangle \rightarrow |1\rangle$ transition. The data is normalized for each flux bias between 0 and 1 for clarity. Insets showing cross sections of the sweep near and far from a splitting.

3.4.1.4 Time domain characterization

Next, we characterize the qubit in the time domain to find its relaxation and coherence times. The following measurements were all performed with zero detuning, and at the same flux bias ($f = 11.25\,\mathrm{GHz}$). In figure 3.9(a) we show the probability P_1 after applying a π pulse and waiting a varying time τ. The decay follows an exponential law, with a decay time[2] $T_1 \simeq 300\,\mathrm{ns}$. In figure 3.9(b) we show P_1 immediately after applying a pulse with varying length τ. This experiment (Rabi oscillations) demonstrates coherent oscillations between the $|0\rangle$ and $|1\rangle$ states. The Rabi frequency in this case is 45 MHz, however Rabi frequencies as high as 400 MHz are attainable with our current pulser. The decay time of the oscillations obtained from a fit to $Ae^{-t/T_R}cos(\omega t + \phi)$ is 192 ns. Using the Torrey solution[14] to the Bloch equations we can deduce the expected *homogeneous* dephasing time: At high Rabi frequencies ($\Omega^2_{Rabi} > \Gamma'_2, \Gamma_1$) and zero detuning, the Rabi oscillations decay at the average rate $\Gamma_R = \frac{1}{2}(\frac{1}{T_1} + \frac{1}{T'_2})$, thus we expect a homogeneous dephasing time $T'_2 \approx 180\,\mathrm{ns}$. This is much longer than the estimation from the linewidth, as expected and should be compared to a spin echo measurement. Figure 3.9(b) shows P_1 immediately after the sequence $\frac{\pi}{2} \rightarrow \tau \rightarrow \frac{\pi}{2}$ where τ is varied, a so called Ramsey experiment. The fringes in this experiment decay at a rate $\Gamma_2 = T_2^{-1} > \Gamma_1/2$. A fit to the same formula as we used earlier gives a decay time of 70 ns. We should point out that the Ramsey fringes do not decay exponentially. In fact, in the absence of relaxation we expect a Gaussian decay[34]. Instead, we follow Yoshihara *et al.*[35]

[2] An interesting fact we discovered is that the decay time can be reduced if the repetition rate (the inverse of time between repeated experiments) is too high. We find that adding a 1 ms waiting time after the experiment can extend the lifetime by about 60 ns. Further increase does not affect the lifetime. We suspect that the creation of non-equilibrium quasiparticle excitations[15] during SQUID switching contributes to this effect, however it requires further investigation.

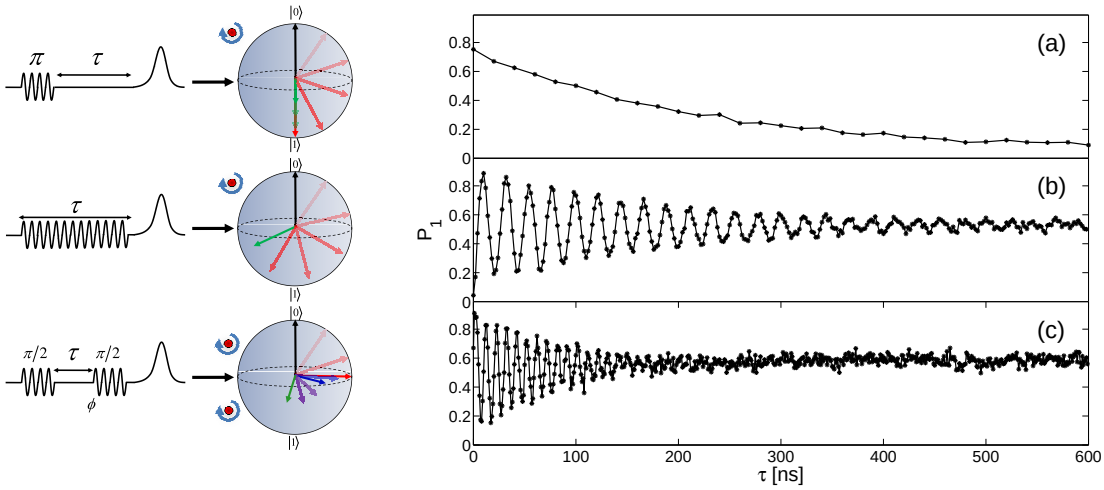

Figure 3.9: Time domain characterization of the qubit. (a) Relaxation (T_1), (b) Rabi oscillations, (c) Ramsey fringes. Left: the sequence used for each experiment and the corresponding evolution of the Bloch vector.

and fit the Ramsey curve to $Ae^{-\Gamma_1/2-(\Gamma_2^\phi t)^2}cos(\omega t+\phi)$, where Γ_2^ϕ is the dephasing rate due to low frequency energy fluctuations and Γ_1 was fixed at 4.5 MHz from earlier measurement. We find the total dephasing time to be 80±10 ns, which is still higher than the linewidth estimation. The large difference between the measurements may be linked to errors we observe at the end of the microwave pulses that result in the Bloch vector shifted from the equator during the free precession in the Ramsey sequence. The fringes in this measurement were emulated by sweeping the phase of the second pulse (relative to the first pulse) along with τ. This demonstrates our control of both phase and amplitude of the microwave signal.

3.4.2 Measuring the qubit

As explained in 1.1.2.2, the probability of the qubit being at a certain energy level is mapped into the probability of the phase being ultimately localized in the qubit well after the short measurement pulse. Since the escape rate extremely dependent on the potential barrier , we measure the probability of being in the $|1\rangle$ state or in higher states, $P(|1,2,...\rangle)$ by simply applying a fast (but still adiabatic relative to the transition frequency) flux bias pulse and measuring the escape probability. In the calibration measurements, the fast pulse was calibrated to yield a 5 % escape probability for the $|0\rangle$ state. This is the point where we expect the maximal visibility (the measure of distinction between the two qubit states)[33]. We expect a 85 % maximum visibility, as indicated from later measurements. This is a remarkably high detection visibility for

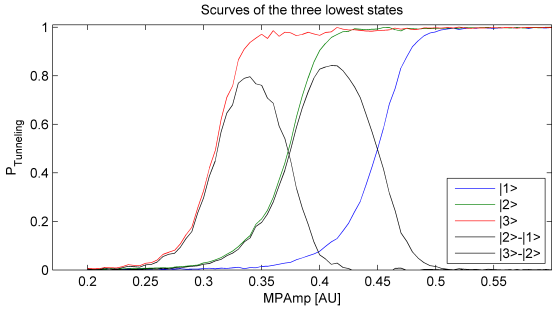

Figure 3.10: Tunneling probability vs. measuring pulse amplitude for the three lowest states and the subtraction between adjacent Scurves. These measurement were done at $f_{01} = 6.5GHz$, $f_{01} - f_{12} = 150$MHz. We can see, that higher state have steeper Scurves, and the gap between the Scurves of two adjacent states decreases.

a single photon at microwave frequency - compared to the quantum efficiency of visible photon detectors, emphasizing the quantum nature of our measurements.
After the general calibration we refine the measurement pulse amplitude (MPA) to yield the maximal visibility specific to a certain flux bias. In order to measure the probability of being in the $|n\rangle$ state or in higher states, $P(|n, n+1, ...\rangle)$, we have to use a MPA that lowers the potential barrier up to a point where states $|n\rangle$ and higher escape out of the well significantly more than states lower than $|n\rangle$. Distinguishing between higher levels requires a lower MPA. For a general initialization state, when we sweep through increasing MPA, lower occupied states can escape from the well, increasing the total escape probability, until we reach the point where the measuring pulse empties the whole well. Measuring the escape probability as a function of increasing MPA should be an increasing monotonous function (regardless of resonant tunneling). For an eigenstate it is “S” shaped, therefore this kind of measurement is called "Scurve". The first step in finding the states occupation is initializing the system to an eigenstate and measuring its Scurve. This should be repeated for each eigenstate in the potential well that can be reached by the drive.

The initialization process of excited eigenstates is obtained by applying a sequential π pulses (after the first resetting process described above). In order to reach a certain state we have to adjust the timing, the driving amplitude and the driving frequency to fit the consecutive transitions. We don’t want the excitation of higher states, therefore, we must use low driving amplitudes which requires long pulses. However, long pulses result in the occupation of lower states as well, due to decoherence. Therefore setting the system to higher states is more complicated and results lower population in the desired state. We can overcome this by finding the fractions of lower states occupation, so that the subtraction of the sum of these fractions times there corresponding Scurves from the original Scurve, create a reasonable Scurve shape. Then we need to re-normalize this

Scurve to fit the range between 0 and 1. The conversion between the escape probability results to the states occupation is done in the following example. We have to solve n equation in n unknowns. The first equation is: $1 = \sum_n P(|n\rangle)$, meaning the conservation of probability . The other equations are: $P_{esc}(MPAi, total) = \sum_n S_{|n\rangle}(MPAi) \times P(|n\rangle)$, meaning the conditional probability. For example, in Fig. 3.10, n=3, and the occupation probabilities follows the equation:

$$\begin{pmatrix} P(|0\rangle) \\ P(|1\rangle) \\ P(|2\rangle) \end{pmatrix} = \begin{pmatrix} 1 & 1 & 1 \\ P_{esc}(MPA1, |0\rangle) & P_{esc}(MPA1, |1\rangle) & P_{esc}(MPA1, |2\rangle) \\ P_{esc}(MPA2, |0\rangle) & P_{esc}(MPA2, |1\rangle) & P_{esc}(MPA2, |2\rangle) \end{pmatrix}^{-1} \begin{pmatrix} 1 \\ MPA1 \\ MPA2 \end{pmatrix}$$

Where $P_{esc}(MPAi, total)$ is the escape probability in MPA=$MPAi$, and $MPAi$ is usually the MPA in the maximal visibility between $|i+1\rangle$ and$|i\rangle$. $S_{|n\rangle}(MPAi)$ is the Scurve of the eigenstate $|n\rangle$ in MPA=$MPAi$. This calculation assumes no excitations to states higher than $|2\rangle$.

3.4.3 Motivation and description of the experiments

In this research we wanted to explore the effect of linearly chirped drive perturbation in anharmonic systems. We conducted a linearly increasing chirp experiment in order to develop a reset technique for preparing the $|1\rangle$ state better than the traditional π pulse (Rabi on resonance). The increasing chirp results can be found in Fig. 4.1, and the Rabi experimental results are shown in Fig. 4.3.
We conducted a linearly decreasing chirp experiment in order to observe the bifurcation phenomenon, whose threshold is supposed to show a transition between classical and quantum regimes. This requires several experiments in different non-linearities, as described in 4.3.

Chapter 4

Results & Discussion

Figures 4.1, 4.3 and 4.4 show the states populations in the qubit well, as a function of the driving amplitude and the driving pulse duration, for a constant bandwidth (600 MHz). These populations are measured at the end of the perturbation for a relative non-linearity $(f_{01} - f_{12})/f_{01} \simeq 2.3\%$ and for a resonance frequency $f_{01} = 6.5$ GHz. The results of each experiment, shown in the figures, are followed by the corresponding numerical simulation. The corresponding simulation was constructed by using the chirp parameters (detuning frequencies, $\delta(t) = \omega_0 - \omega_{ext}(t)$), the 2D sweep parameters (ranges of pulse duration and amplitude magnitude), and the experimental parameters (resonance frequencies ($f_{01}, \frac{f_{02}}{2}$), decay times (T_1, T_2) and the fitted circuit parameters (I_0, C and L)). In order to find the driving amplitude in Rabi frequency (MHz), we took the Furrier transform of each vertical column of the Rabi experiment.

4.1 Linearly increasing chirped drive

In Fig. 4.1 (Top), we can see that the linearly increasing chirp is characterized mainly by the magnitude of the driving amplitude. At low amplitudes, there is no excitation. High amplitudes result in an excitation to states $|2, 3...\rangle$. In the intermediate range, the first excited state has islands of high population in . The simulation results (Fig. 4.1-Bottom) coincide with the experimental results. According to the simulation results, states higher than $|2\rangle$ are not occupied (not shown in the figure).

These results can be explained by the existence of two competing processes: a transition between $|0\rangle$ and $|1\rangle$, and a transition between $|0\rangle$ and $|2\rangle$. In a two level system only first process occurs around the resonant frequency f_{01} .Under the conditions of our experiment, the driving frequency passed through the frequency $f_{02}/2$ before f_{01} which can result in a two-photon transition. The latter process is dominant in high amplitudes, while the first one is dominant in intermediate amplitudes. None of them

is dominant in low amplitudes.

Applying the linearly increasing chirped drive on the ground state leads to the occupation of the first excited state. This method is, in fact, a reset technique. At this point, we would like to compare the chirped drive method to the Rabi -π pulse method, which uses a resonant drive (see Fig. 4.3). We can see that the chirp method is more robust than the Rabi π pulse method, meaning that its sensitivity to changes in the driving amplitude is significantly lower. On the other hand, because of the two-photon transition, the population of the first excited state is not high enough. This can be improved by starting the chirp after the two-photon frequency, as can be seen in the simulation (Fig. 4.2). There is a large area with quite high population in the first excited state (85%), which has a very low sensitivity to changes both in the driving amplitude and in the pulse duration. We can see that the probability of the second excited state becomes higher with the increase of the driving amplitude, but still remains very low. According to the simulation results, states higher than $|2\rangle$ are not occupied.

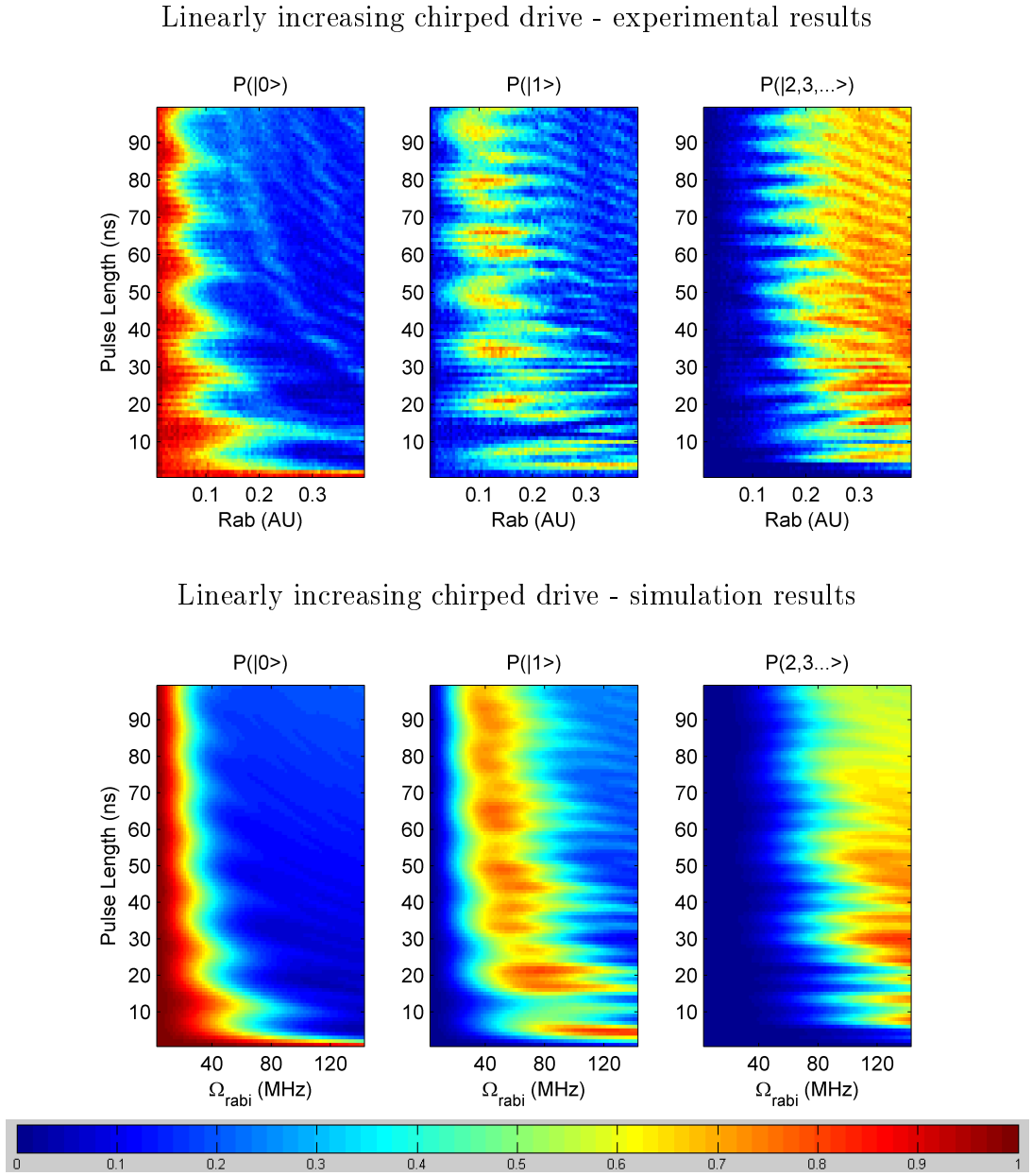

Figure 4.1: States occupation probabilities vs. driving amplitude and driving duration: $f_{01} = 6.5GHz,\ f_{01} - f_{12} = 150MHz,\ \delta_{initial} = 0.04\omega_0\ and\ \delta_{final} = -0.04\omega_0$

4.2 Resonant drive

The Rabi experiment was done for three reasons. The first one is for the calibration of the system, i.e. repeating a known phenomenon experiment helps us ensure that the system works properly. The second reason is to find the conversion of the X axis (the driving pulse amplitude) from arbitrary units to Rabi frequency in MHz. This is

Asymmetrical linearly increasing chirped drive - simulation results

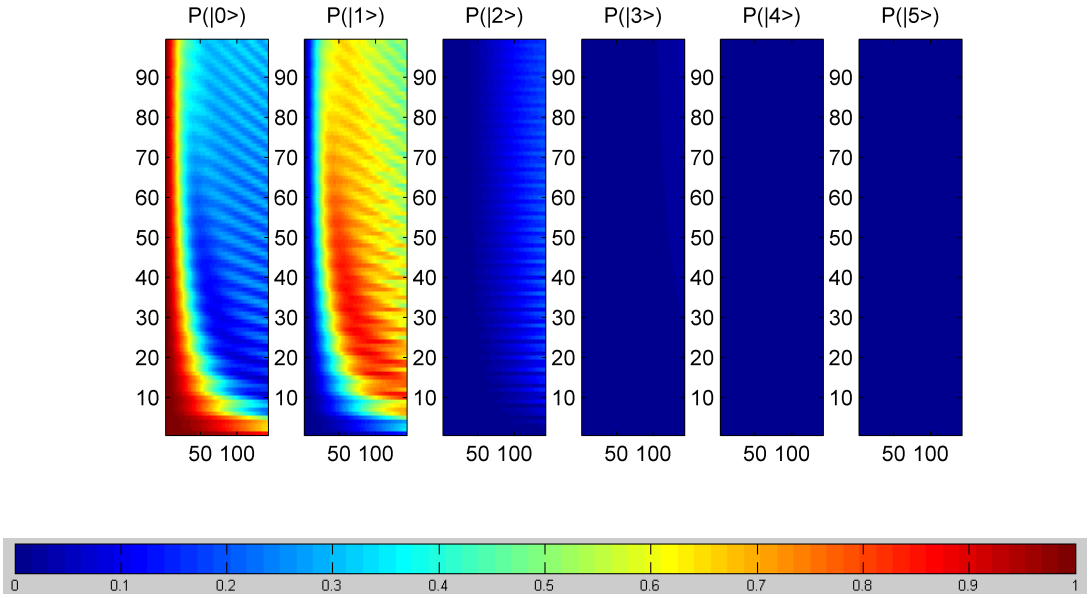

Figure 4.2: States occupation probabilities vs. driving amplitude and driving duration: $f_{01} = 6.5GHz,\ f_{01} - f_{12} = 150MHz,\ \delta_{initial} = 0.022\omega_0$ *and* $\delta_{final} = -0.068\omega_0$

done by Fourier transform of the Rabi experiment along vertical lines in Fig. 4.3. The resulting units conversion ratio is: 1 AU = 355 MHz. This conversion ratio is valid to all measurements that have the same non linearity (flux bias). The third reason is the comparison between the Rabi oscillations and the increasing chirp as two reset techniques that prepare the $|1\rangle$.

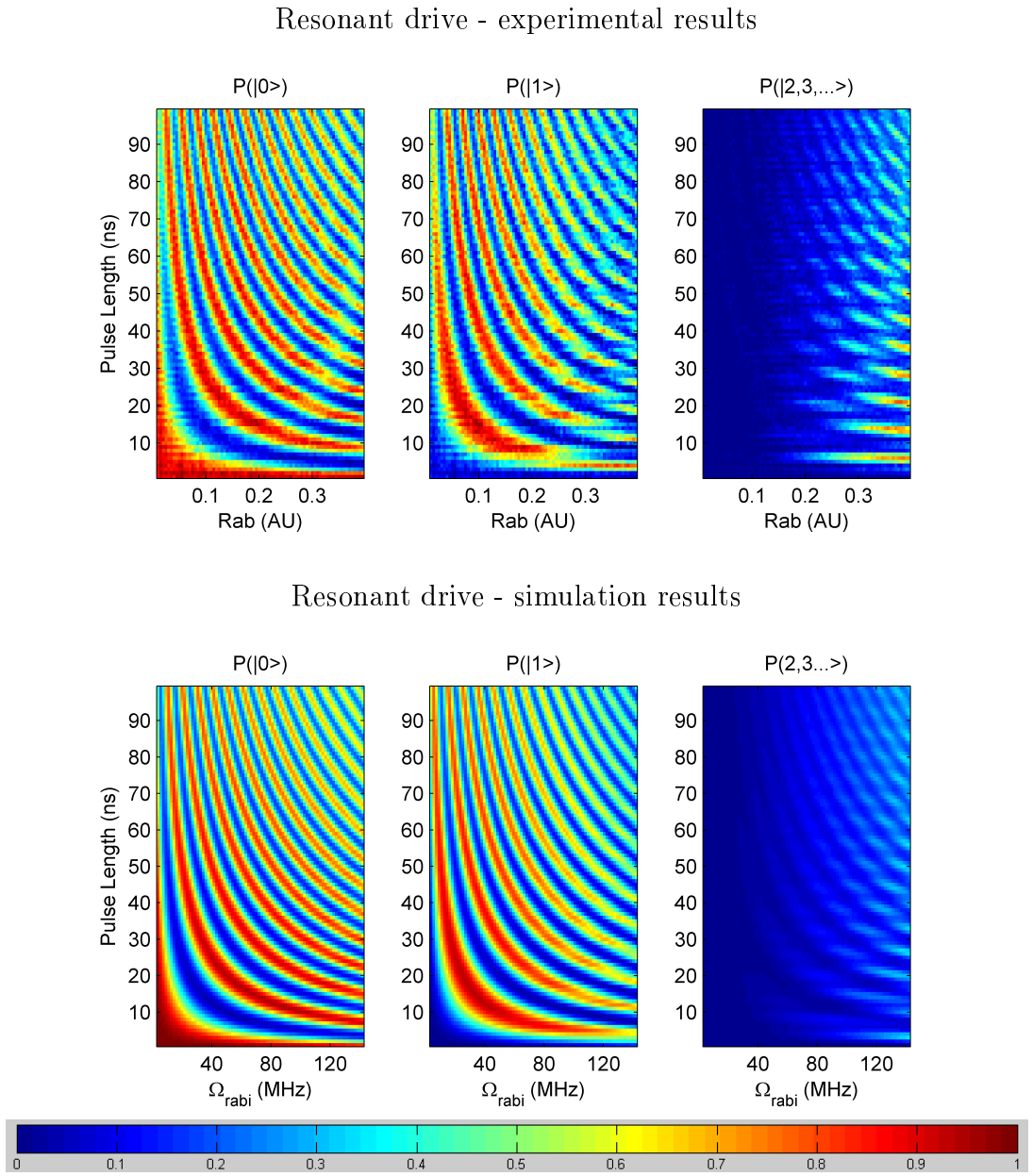

Figure 4.3: States occupation probabilities vs. driving amplitude and driving duration: $f_{01} = 6.5GHz,\ f_{01} - f_{12} = 150MHz,\ \delta(t) = 0$

4.3 Linearly decreasing chirped drive

The results of the linearly decreasing chirp experiment (Fig. 4.4, top) show the existence of a threshold phenomenon. Beyond the threshold, the system is excited to states higher than $|1\rangle$, while below it there is no significant excitation, as we expected. The simulation results (Fig. 4.4, bottom) coincide with the experimental results.

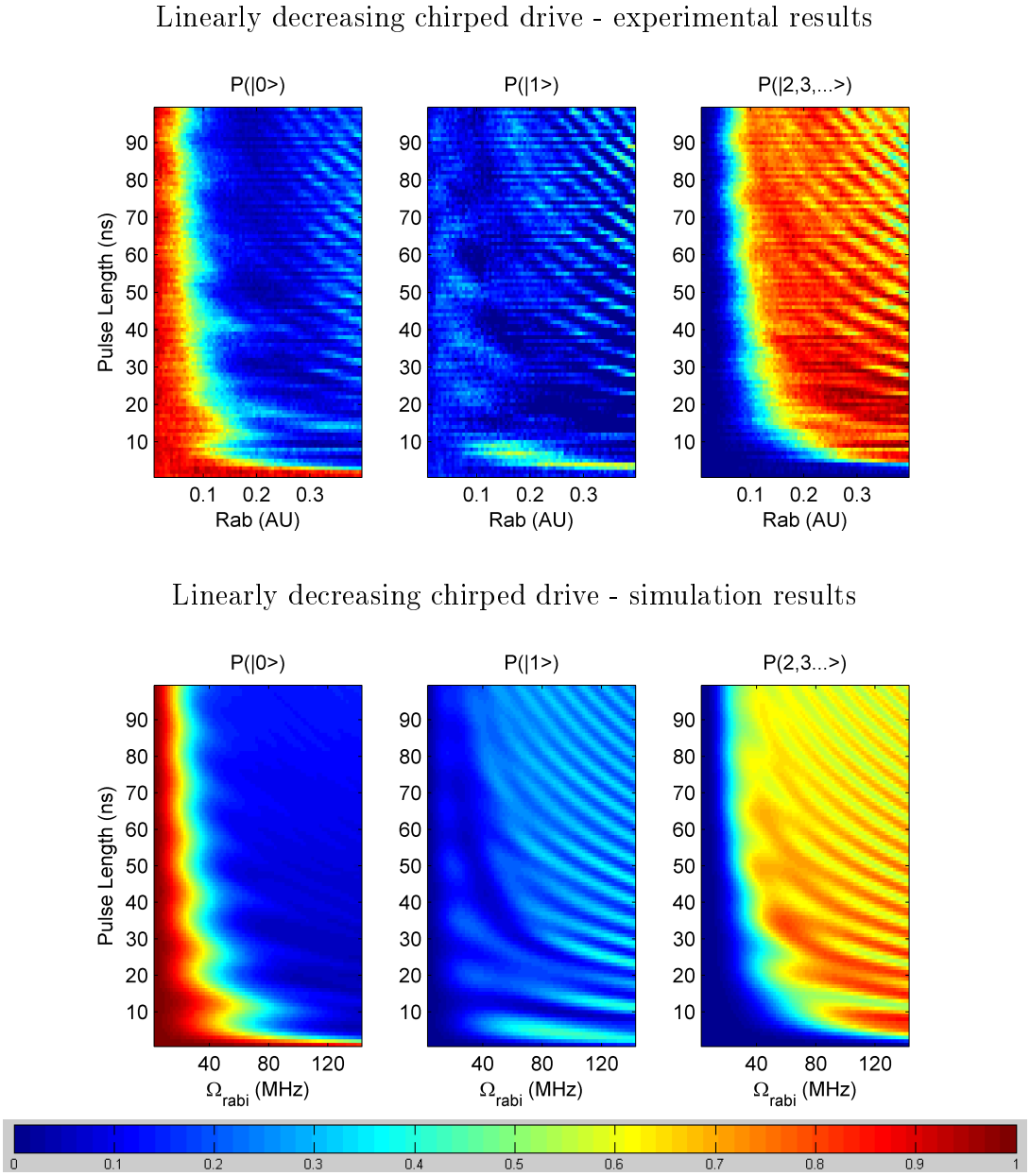

Figure 4.4: States occupation probabilities vs. driving amplitude and driving duration: $f_{01} = 6.5GHz,\ f_{01} - f_{12} = 150MHz,\ \delta_{initial} = -0.04\omega_0\ and\ \delta_{final} = 0.04\omega_0$

We wanted to map also the more classical regime; therefore we conducted another set of the linearly decreasing chirp experiments in a lower nonlinearity (Fig. 4.5). This set of experiments was measured at a specific measuring pulse amplitude (MPA), calibrated so that the bifurcation cutoff would be at middle of the energy levels that can be excited by the drive. In this way the escape probability is, in fact, the "latching" probability. Here, we didn't measure the states occupation because we it is impossible to generate the pure eigenstates using sequential π pulses in such a nonlinearity. The

Linearly decreasing chirp- experimental results

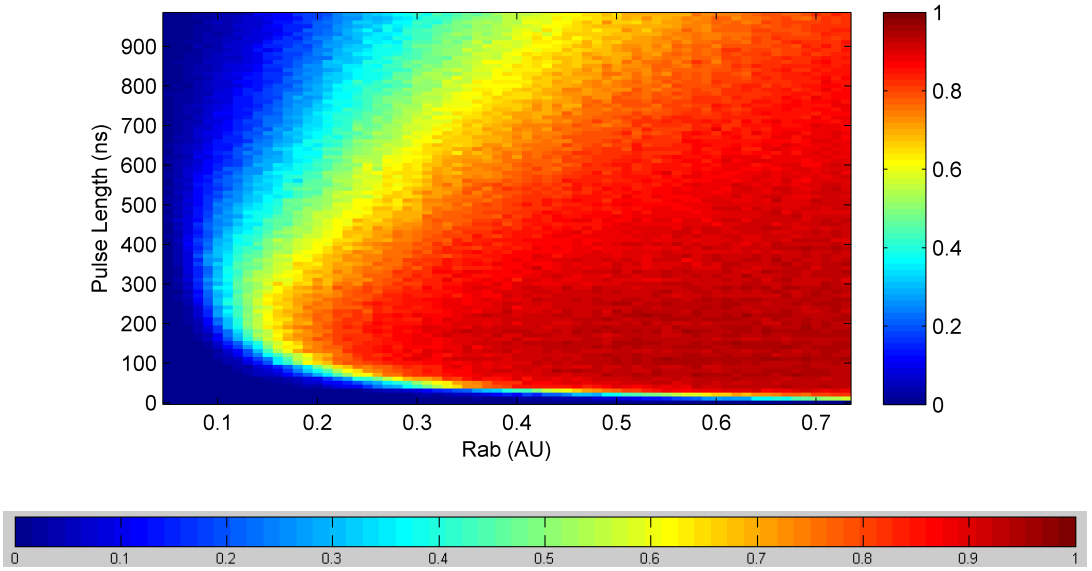

Figure 4.5: The "latching" probability at MPA calibrated to the middle of the relevant energy range: $f_{01} = 9.056GHz,\ f_{01} - f_{12} = 20MHz,\ \delta_{initial} = 0.0375\omega_0$ *and* $\delta_{final} = -0.0375\omega_0$;
The conversion of the X axis is more complicated in this low nonlinearity but we can still see quality measures.

measurements show a threshold phenomenon. Looking at long time intervals, we can see that the threshold expands and shifts to the right. This can be explained by a decoherence effect. The critical time is around the coherence time.

The bifurcation phenomenon was examined by measuring the probability of staying in the branch where the oscillator phase-locks to the chirped drive (the "latching" probability). In order to compare experiments conducted under different conditions, we present our data in the characteristic dimensionless parameter space (P_1 and P_2) (discussed in 1.2.5.3), which is a transformation of the experimental parameter space (nonlinearity, driving amplitude and driving duration).

In the case of the higher nonlinearity we treated the probability of $|2, 3, ...\rangle$ as the "latching" probability (as explained in 1.2.5.2). This is a good approximation, since we can see that $|1\rangle$ is only slightly populated and can serve as the bifurcation cutoff. Using different definitions for the bifurcation cutoff such as: the measurement pulse amplitudes of maximal visibilities between adjacent states, MPA1 and MPA2, yields similar results. The problematic area is around the blob at short times, where the three different definitions show a discrepancy (not shown in this work). In the case of the lower nonlinearity we measured the "latching" probability from the beginning. In Fig. 4.6 we can see the "latching" probability of the previous two experiments (4.4 and 4.5).

When we combine the bifurcation results of the two non-linearities, the threshold of bifurcation shows a transition between the quantum regime and the classical regime.

In this system there is a difficulty to define exactly where is the right energy cutoff in which states having higher energy are "latched" (phase locked) by the chirped drive, and the rest are not. The difficulty stems from the fact that the bifurcation is not always complete at the end of the perturbation. The following experimental limitations contribute to the incomplete bifurcation. The duration of the drive pulse must be shorter than the coherence time. Our chirp bandwidth is limited ($\sim$600MHz) for technical reasons, as is our driving pulse amplitude.

Another experiment that could enhance our understanding of the bifurcation phenomenon is the chirp dynamics, which tracks the states' population at different times along the chirp. This experiment should show the transition between the sequential state excitation characterizing the ladder climbing and the Poisson distribution of occupied states (coherent-like states) characterizing the autoresonance. The conduction of such an experiment requires developing a new method to measure the states occupation. We believe that the Scurves measurements and their derivatives can be a key to achieving this goal. Fig. 4.7 is an example of such measurements that have been done recently.

"Latching" probability- experimental results

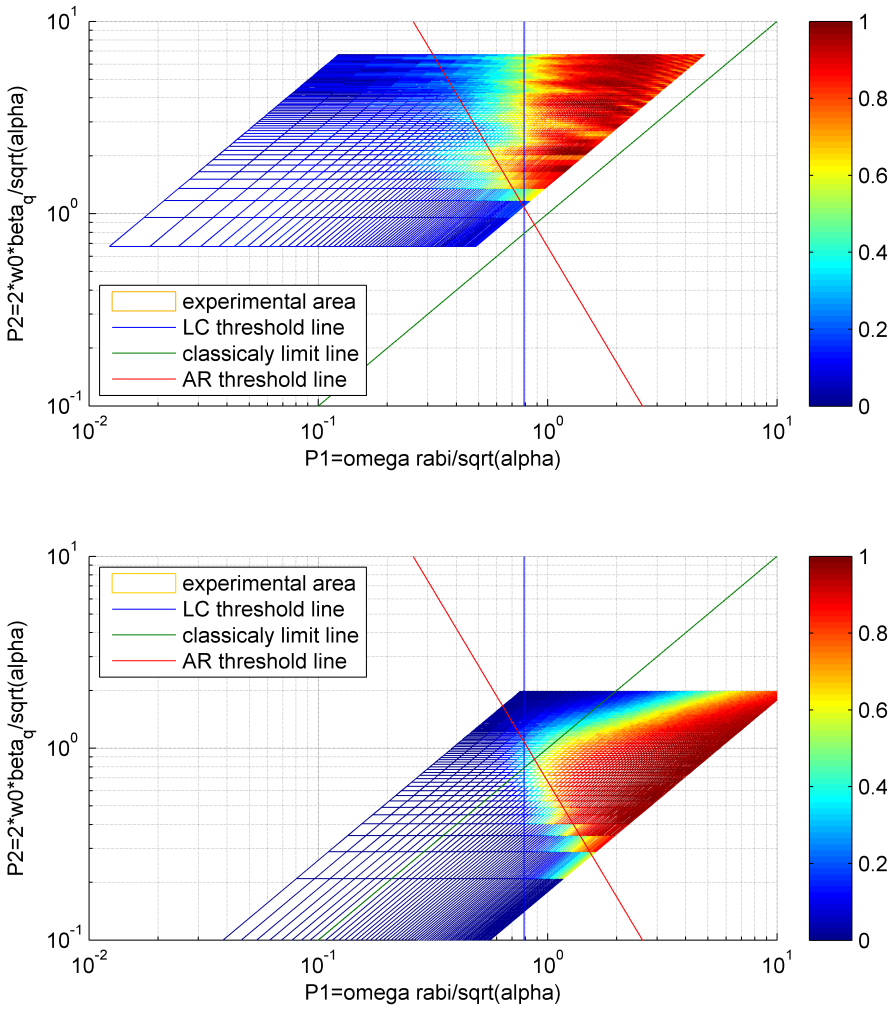

Figure 4.6: Experimental results in the dimensionless parameter space: Top-Decreasing chirp for relative nonlinearity=2.3% ; Bottom-Asymmetrical decreasing chirp for relative nonlinearity=0.2% . The bottom figure has an arbitrary X scale.

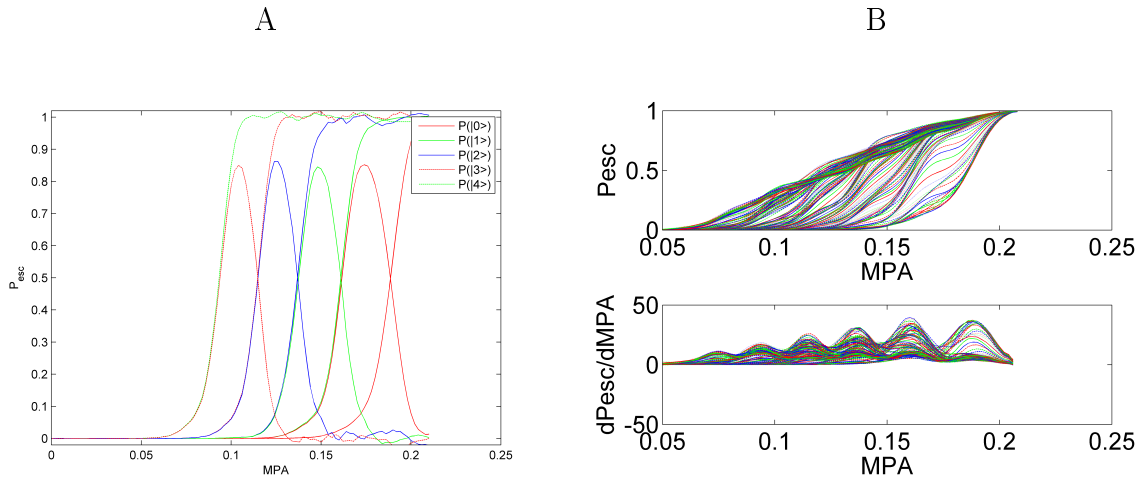

Figure 4.7: A: Scurves of the 5 lowest states. B: Top - Scurves for different measurement pulse amplitudes having the same pulse length. This is a transection of the 3D Scurve, meaning, the escape probability for each driving amplitude, driving duration (pulse length) and measurement pulse amplitude (MPA). Bottom - The minima of the Scurves' derivatives give an indication of the maximal visibilities.

Chapter 5

Summary & Outlook

Superconducting Josephson phase circuits act like anharmonic oscillators. Their remarkable property of tunable nonlinearity enables conducting experiments both in quantum and in classical regimes. A shallow potential barrier is characterized by high nonlinearity, which allows the quantum ladder climbing (sequential state excitation) to be observed. As the potential barrier gets deeper it can no longer be approximated as cubic potential but is better approximated as quadratic potential, allowing the classical autoresonance (the population of coherent-like states) to be observed.

In this work we experimentally mapped the classical, quantum and also the intermediate regimes of a driven nonlinear oscillator. We examined the bifurcation phenomena by measuring the probability of staying in the branch where the oscillator phase-locks to the chirped drive. The measurements are consistent with numerical simulations, and the bifurcation threshold shows a good match with the theoretical threshold curves of the quantum ladder climbing and the classical autoresonance. In fact, a continuous transition between classical and quantum dynamics is obtained.

Our second goal was to develop numerical and experimental methods for working with anharmonic oscillators. We simulated a realistic anharmonic oscillator, in order to develop coherent control methods. The simulation fits both theoretical calculations and experimental results, and therefore we believe it is a good tool for future applications as well.

Applying a positive chirped drive can be used as a reset technique. The advantage of this technique is that it shows robustness to changes in the driving amplitude. The main disadvantage of this technique is that in the non-linearity which we worked, the multi-photon transition was too dominant, because its frequency was too close to the resonance frequency. However, going to higher non-linearity should suppress it.

In future research we would like to sharpen the distinction between the quantum and classical regimes and show a more detailed description of the bifurcation threshold. This

can be done by refining the bifurcation cutoff, in order to validate it for a broader range around the expected threshold in the dimensionless parameter space. We want to extend the experiments so that different overlapping areas in the parameter space will show a consistent threshold curve. As a result of both the analytical and numerical analysis, we expect significant oscillations in the intermediate regime (where the theoretical lines intersect) in a finite LZ manner.

From this work, we can see that the flux bias Josephson circuits give a good experimental environment for enhancing our understanding of fundamental decoherence physics. The quantum and classical phenomena can be distinguished and controlled.

Bibliography

[1] J. Clarke and F. K. Wilhelm. Superconducting quantum bits. 2008.

[2] J Clarke J. M. Martinis, M. H. Devoret. Experimental tests for the quantum behavior of a macroscopic degree of freedom: The phase difference across a josephson junction. *Phys. Rev. B*, 1987.

[3] L. N. Cooper J Bardeen and J.R. Schrieffer. Theory of superconductivity. *Phys. Rev.*, 108:1175–1204, 1957.

[4] Michael Tinkham. *Introduction to Superconductivity: Second Edition (Dover Books on Physics)*. Dover Publications, June 2004.

[5] B. D. Josephson. Coupled superconductors. *Rev. Mod. Phys.*, 1964.

[6] M. H. Devoret. Quantum fluctuations in electrical circuit. *Les Houches, Session LXIII*, 1995.

[7] A. Wallraff M. H. Devoret and J. M. Martinis. Superconducting qubits: A short review. *Arxiv preprint cond-mat/0411174*, 2004.

[8] Jens Koch, Terri M. Yu, Jay Gambetta, A. A. Houck, D. I. Schuster, J. Majer, Alexandre Blais, M. H. Devoret, S. M. Girvin, and R. J. Schoelkopf. Charge-insensitive qubit design derived from the cooper pair box. *Physical Review A (Atomic, Molecular, and Optical Physics)*, 76(4):042319, 2007.

[9] T. A. Fulton and L. N. Dunkleberger. Lifetime of the zero-voltage state in josephson tunnel junctions. *Phys. Rev. B*, 9, 1974.

[10] John M. Martinis, Michel H. Devoret, and John Clarke. Energy-level quantization in the zero-voltage state of a current-biased josephson junction. *Phys. Rev. Lett.*, 55(15):1543–1546, Oct 1985.

[11] R. Rouse, Siyuan Han, and J. E. Lukens. Observation of resonant tunneling between macroscopically distinct quantum levels. *Phys. Rev. Lett.*, 75(8):1614–1617, Aug 1995.

[12] Michel H. Devoret, John M. Martinis, and John Clarke. Measurements of macroscopic quantum tunneling out of the zero-voltage state of a current-biased josephson junction. *Phys. Rev. Lett.*, 55(18):1908–1911, Oct 1985.

[13] John M. Martinis, S. Nam, J. Aumentado, and C. Urbina. Rabi oscillations in a large josephson-junction qubit. *Phys. Rev. Lett.*, 89(11):117901, Aug 2002.

[14] L. Allen and J. H. Eberly. *Optical Resonance and Two-Level Atoms.* Dover Publications, December 1987.

[15] M. Antsmann J M, Martinis and J. Aumentado. Energy decay in josephson qubits from non-equilibrium quasiparicles. *arxiv*, 2009.

[16] R. W. Simmonds, K. M. Lang, D. A. Hite, S. Nam, D. P. Pappas, and John M. Martinis. Decoherence in josephson phase qubits from junction resonators. *Phys. Rev. Lett.*, 93(7):077003, Aug 2004.

[17] Matthew Neeley, M. Ansmann, Radoslaw C. Bialczak, M. Hofheinz, N. Katz, Erik Lucero, A. O'Connell, H. Wang, A. N. Cleland, and John M. Martinis. Transformed dissipation in superconducting quantum circuits. *Physical Review B (Condensed Matter and Materials Physics)*, 77(18):180508, 2008.

[18] Michael A. Nielsen and Isaac L. Chuang. Quantum computation and quantum information. October 2000.

[19] Radoslaw C. Bialczak, R. McDermott, M. Ansmann, M. Hofheinz, N. Katz, Erik Lucero, Matthew Neeley, A. D. O'Connell, H. Wang, A. N. Cleland, and John M. Martinis. 1/f flux noise in josephson phase qubits. *Physical Review Letters*, 99(18):187006, 2007.

[20] S. Sendelbach, D. Hover, A. Kittel, M. Muck, John M. Martinis, and R. McDermott. Magnetism in squids at millikelvin temperatures. *Physical Review Letters*, 100(22):227006, 2008.

[21] G. Wendin and V.S. Shumeiko. Superconducting quantum circuits, qubits and computing. *Preprint cond-mat*, 05087929, 2005.

[22] N.V. Vitanov and B.M. Garraway. Landau-zener model: Effects of finite coupling duration. *Phys. Rev. A*, 53, 1996.

[23] L. Friedland G. Marcus and A. Zigler. From quantum ladder climbing to classical autoresonance. *Phys. Rev. A*, 69, 2004.

[24] J M. Martinis. Mapping of flux-bias to current-bias circuits in a phase qubit. Private Communication, 2003.

[25] Matthias Steffen, John M. Martinis, and Isaac L. Chuang. Accurate control of josephson phase qubits. *Phys. Rev. B*, 68(22):224518, Dec 2003.

[26] C. Zener. Non-adiabatic crossing of energy levels. *Proc. R. Soc. London A*, 137:696, 1932.

[27] M. Abramowitz and I.A. Stegun. *Handbook of Mathematical Functions.* Dover, New York, 1964.

[28] E. Sarid I. Barth, L. Friedland and A.G. Shagalov. Autoresonant transition in the presence of noise and self-fields. *Phys. Rev. Lett.*, 2009.

[29] L. Friedland J. S. Wurtele O. Naaman, J. Aumentado and I. Siddiqi. Phase-locking transition in a chirped superconducting josephson resonator. *Phys. Rev. Lett.*, 101:117005, 2008.

[30] A. Zigler G. Marcus and L. Friedlan. Molecular vibrational ladder climbing using a sub-nanosecond chirped laser pulse. *Europhys. Lett.*, 74 43, 2006.

[31] G. A. Keefe F. P. Milliken, J.R. Rozen and R. H. Koch. 50 ohm characteristic impedance low-pass metal powder filters. *Rev. Sci. Instrum.*, 78, 024701, 2007.

[32] K. B. Cooper, Matthias Steffen, R. McDermott, R. W. Simmonds, Seongshik Oh, D. A. Hite, D. P. Pappas, and John M. Martinis. Observation of quantum oscillations between a josephson phase qubit and a microscopic resonator using fast readout. *Phys. Rev. Lett.*, 93(18):180401, Oct 2004.

[33] Erik Lucero, M. Hofheinz, M. Ansmann, Radoslaw C. Bialczak, N. Katz, Matthew Neeley, A. D. O'Connell, H. Wang, A. N. Cleland, and John M. Martinis. High-fidelity gates in a single josephson qubit. *Physical Review Letters*, 100(24):247001, 2008.

[34] John M. Martinis, S. Nam, J. Aumentado, K. M. Lang, and C. Urbina. Decoherence of a superconducting qubit due to bias noise. *Phys. Rev. B*, 67(9):094510, Mar 2003.

[35] F. Yoshihara, K. Harrabi, A. O. Niskanen, Y. Nakamura, and J. S. Tsai. Decoherence of flux qubits due to 1/f flux noise. 2006.

תקציר

בשנים האחרונות, יש עניין גובר במערכות קוונטיות ברות שליטה הן לצורך לימוד של פיסיקה בסיסית של איבוד קוהורנטיות (decoherence) והן בשביל האפשרות ליצור התקנים חישוביים יעילים. המעבדה שלנו מתמקדת ביישום מערכת קוונטית במצב מעובה, המבוססת על מעגלי העל-מוליכות של ג'וספסון (Josephson circuits). מעגלים אלו מיוצרים בשיטות ליטוגרפיה ודיפוזיציה המושאלות מתעשיית המוליכים למחצה. מעגלי העל-מוליכות מתאפיינים ומתייחדים בהעדר דיסיפציה, שהיא תכונת מפתח לצפייה בתהליכים קוונטיים במערכת פיזיקאלית.

ידוע כי כאשר אוסילטור הרמוני קוונטי נמצא במצב קוהרנטי הוא מתנהג כמו מקבילו הקלאסי. למעשה, זה מה שמתקבל כאשר אנחנו מעוררים רזונטור באמצעים קלאסיים. על מנת לייצר מצבים לא קלאסיים באמצעים קלאסיים, מה שדרוש הוא רכיב לא ליניארי במערכת. צומת ג'וספסון הוא רכיב שמאופיין בתכונה זו.

אוסצילטורים לא הרמוניים מגיבים באופן ייחודי לכוח מאלץ בתדר יורד דינאמית ,וניתן להתייחס אל תגובה זו כאל אוטורזוננס או טיפוס בסולם (ladder climbing) במשטרים קלאסיים או קוונטיים בהתאמה. באופן טיפוסי, מתחרשת ביפורקציה באכלוס רמות האנרגיה כתלות הן באמפליטודת הכוח המאלץ והן באי-לינאריות של המערכת. במרחב פרמטרים זה, מצופה לראות מעבר ברור בין משטר קלאסי למשטר קוונטי בסף הביפורקציה. מחקרים קודמים התייחסו לכל אחד מהמשטרים הללו בנפרד, וחקרו מערכות רק באחד מהתנאים הנ"ל.

המטרה המרכזית במחקר זה, היא למפות את שני המשטרים נסיונית, וכן לכלול את משטרי הביניים. מעגלי העל-מוליכות של ג'וספסון מסוגלים לעשות זאת הודות לכך שהם מאפשרים ויסות של האי-לינאריות. אנו מראים מדידות של תופעות הביפורקציה במערכת זו על גבי טווח פרמטרים נרחב, וניתן לראות את המעבר המצופה. אנו משווים תוצאות אלו לסימולציות נומריות ולחישובים אנליטיים.

המטרה השניה היא לפתח שיטות המאפשרות שליטה במערכת הקוונטית המאופיינת באיבוד קוהרנטיות גובר עם הזמן. בעבודה זו אנו מראים טכניקת אתחול המשתמשת בכוח מאלץ בתדר

משתנה דינאמית (chirped drive), שבהשוואה לאילוץ בתדר רזוננטי מאופיינת ברגישות הרבה יותר נמוכה לאמפליטודת האילוץ.
מטרה נוספת של עבודה זו היא לתת ניתוח משמעותי, הן אנליטי והן נומרי, וכך ליצור סימולציות ריאליסטיות עבור מעגלי העל-מוליכות של ג'וספסון, ובמיוחד עבור מעגלי פאזה נשלטי שטף (Flux bias phase circuits).

תזה זו מורכבת מחמישה פרקים. הפרק הראשון מכיל רקע תיאורטי קצר כהקדמה לעבודתי, ולאחריו ניתוח אנליטי ונומרי שסיכמתי, ערכתי ופיתחתי. הפרק השני מציג את שיטות העבודה ואת המערכות עליהן נערכו הניסויים. הפרק השלישי מראה את התוצאות הניסיוניות. הפרק רביעי מכיל דיון מפורט על תוצאות הניסוי, וכן את השלבים הדרושים לפיתוח עתידי של המחקר. הפרק האחרון מכיל סקירה מסכמת, והערות המסכמות את העבודה.

האוניברסיטה העברית בירושלים

הפקולטה למתמטיקה ולמדעי הטבע

מכון רקח לפיסיקה

מעבר בין אוטורזוננס לבין טיפוס בסולם במעגלי ג'וספסון

מגישה: יערה רופא
מספר זהות: 039884945

מנחה: ד"ר נדב כ"ץ

עבודת גמר לתואר מוסמך במדעי הטבע

כסלו התשע"א